ABSTRACT

Title of Document:	INVESTIGATIONS INTO THE EFFECTS OF SECONDARY-FREQUENCY ADDITIONS ON SLENDER ROTATING STRUCTURES
	Gregory William Meyer, Master of Science, 2014
Directed By:	Professor Balakumar Balachandran Department of Mechanical Engineering

Drill strings are slender structures used extensively in drilling and mining operations. In this thesis work, secondary-frequency input additions to the drive speed input are considered and the resulting influence on system dynamics is examined. Experimental studies are conducted with a laboratory scale drill-string arrangement, and high-frequency and low-frequency additions are considered for cases in which the drive speed frequency is close to either a bending mode or torsion mode natural frequency. It is found that carefully chosen secondary-frequency additions can be used to attenuate undesirable system dynamics, especially, for rotary systems. To complement the experiments, numerical studies are conducted with a reduced-order model of the drill-string system. The obtained numerical results are found to be in reasonable agreement with the experimental results. Preliminary numerical results obtained in the presence of rotor-stator interactions are also included. In addition, areas in which the model construction will need further development are also discussed. The findings of this work can be useful for

considering secondary-frequency addition based schemes for controlling bending and torsional motions of drill-string systems.

INVESTIGATIONS INTO THE EFFECTS OF SECONDARY-FREQUENCY
ADDITIONS ON SLENDER ROTATING STRUCTURES

By

Gregory William Meyer.

Thesis submitted to the Faculty of the Graduate School of the
University of Maryland, College Park, in partial fulfillment
of the requirements for the degree of
Master of Science
2014

Advisory Committee:
 Professor B. Balachandran, Chair and Advisor
 Professor J. Hubbard, Aerospace Engineering
 Associate Professor N. Chopra, Mechanical Engineering

Acknowledgements

I would like to thank Professor Balachandran, my advisor and committee chair, for his support and guidance during my graduate studies. I want to thank Nick Vlajic for helping me with my research. I also want to thank all of my other colleagues in the Dynamics and Vibrations Group for their support and help. Finally, I would like to thank my family and friends for their love and the encouragement they constantly provided.

Table of Contents

List of Tables

List of Figures

vi

Chapter 1

Introduction

A drill string is a slender hollow pipe used in drilling operations to transmit power from motors on or near the surface to the drill bit located at its end. These slender and flexible structures are used extensively in modern drilling operations and have several interesting applications, include directional drilling, an example of which is depicted in Figure 1.1. Drill-string dynamics exhibit a variety of nonlinear phenomena due to the nature of their interactions with the surrounding environment. These phenomena include stick-slip interactions between the drill string and the borehole, forward whirling, and backward whirling. Stick-slip motions occur when a part of the drill string, usually the drill bit or a part of the string in contact with the borehole wall, is temporarily stopped by contact forces at the point of interaction and speeds back up again when the frictional force is overcome. As a consequence, the string can undergo torsion and experience large amplitude torsional vibrations when the string suddenly speeds up after it is freed from the wall. Forward whirling occurs when the drill string comes into contact with the borehole wall and begins rotating along the wall in the same direction as the drive speed; in this mode, slipping is possible between the borehole wall and the string. Backward whirling is similar, except that the string whirls in a direction opposite its drive speed. Backward whirling is typically associated with high stress levels in the structure. Modeling of these motions and control of the same have been the focus of many previous and current studies on drill-string dynamics.
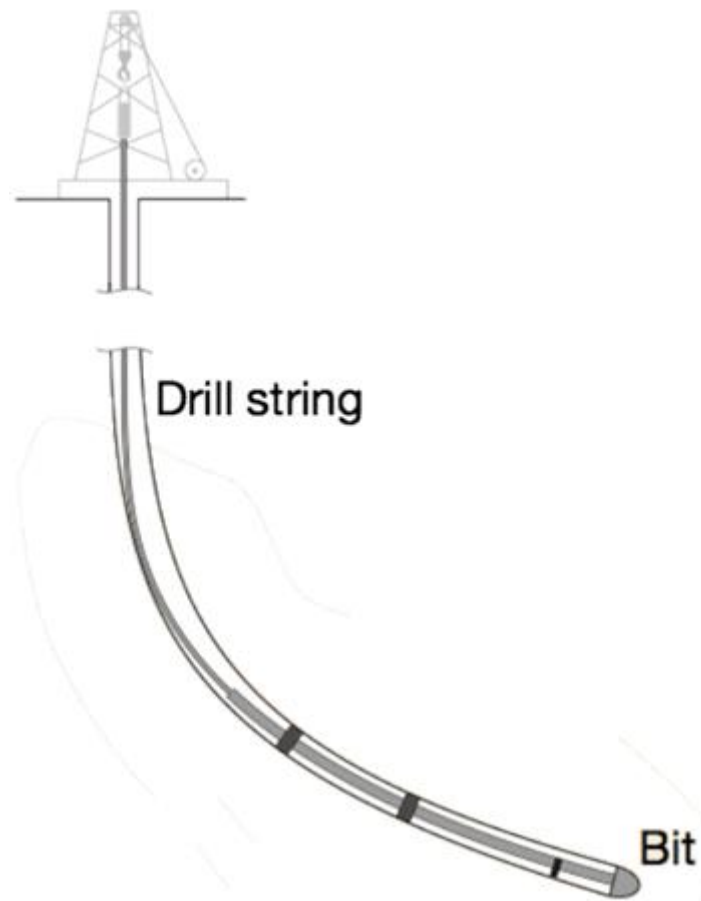
Figure 1.1. An example of horizontal or curved drilling (adapted from:

http://www.cefor.umn.edu/research/numerical-simulation-tools/directional-drilling/).

1.1 Configuration of a Typical Drill String

Typically, a drill string consists of a shaft of drill piping, a drill bit, a drill collar and stabilizers. A configuration for a standard drilling operation is illustrated in Figure 1.2. The drill string is supported by a rig and hoisting system, which is used to control the tension in the drill string and, in effect, the weight on the drill bit. Torque
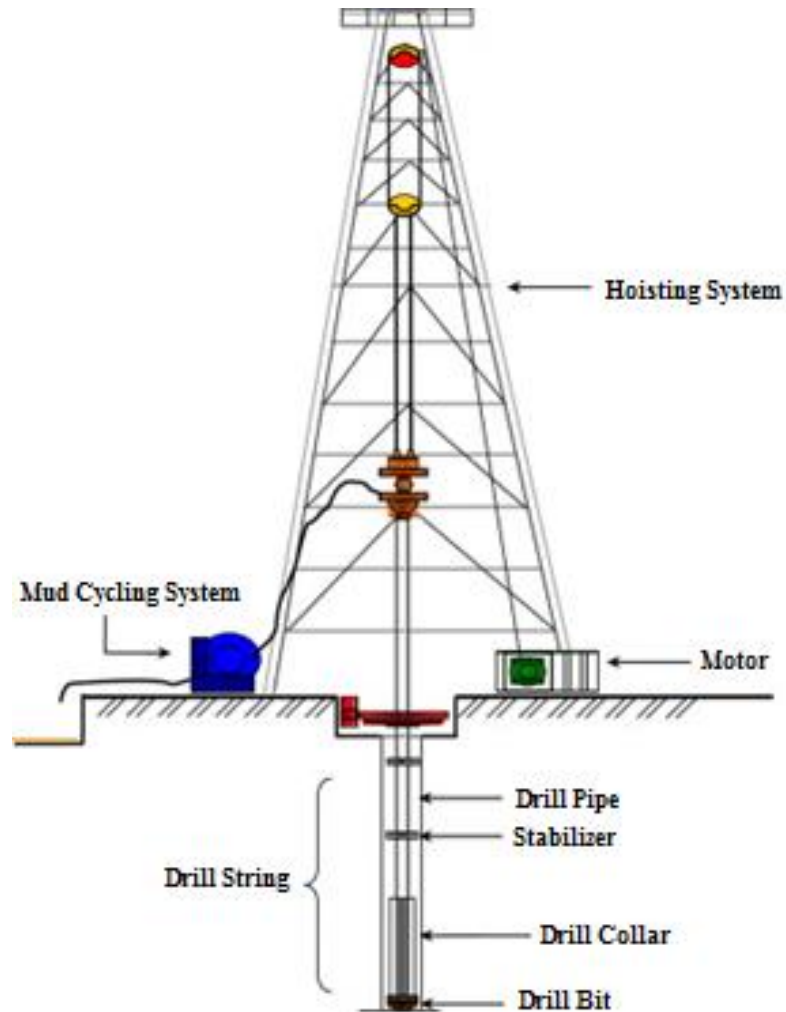
Figure 1.2. Illustration of a typical drill rig assembly (Adapted from Liao,

Balachandran, Karkoub, and Abdel-Magid, 2011).

is transmitted from a motor through the rig to the drill string, and then, through the

drill string to the drill bit. The major portion of the drill string consists of drill piping,

a series of long metal tubes connected together. Throughout the drilling process, a

viscous fluid referred to as drill mud is pumped through the drill piping to the drill bit.

Drill mud serves two important functions in a drilling operation. First, the mud acts

as a coolant to prevent the drill string from overheating. Second, the mud washes

away the rocks and earth broken up by the drill bit and the motion of the drill string

forces the resulting slurry to the surface. The mud can then be reused for future

operations. The drill collars are sections of the drill string near the drill bit. These

sections of the drill string near the drill bit that are thicker in diameter and heavier in

weight then the drill piping. This allows them to withstand high stresses that tend to

occur near the drill bit while the rig is in operation. The final piece of the drill-string

assembly is the stabilizer. These are sections of the drill string that are wider than the

drill collars, but they do not extend along the length of the drill string. The stabilizers

serve the purpose of limiting the amplitude of the lateral oscillations of the drill string

by coming into contact with the borehole wall with only small oscillations of the drill

string. This generates a restoring force that limits the oscillations of the rest of the

drill string.

1.2 Literature on Modeling and Control of Drill-String Dynamics

Multiple studies have been devoted to the modeling and control of drill-string

systems. In terms of modeling, most studies favored the use of reduced-order models

to simulate the interactions between some aspect of the drill string, usually the drill

bit or collars, and the borehole well being drilled. Most attempts to control the

dynamics of the drill string have focused on controlling the torsional vibrations of the

system through a variety of closed loop controllers.

Jansen (1991) proposed a two degree-of-freedom model in which the drill-

string system is treated as a rotating disk with an unbalanced mass enclosed within a

borehole. Interactions between the drill sting and stabilizer were modeled as a spring

force acting on the center of the disk with respect to the location of the stabilizer. Likewise, the interactions between the drill string and borehole wall were modeled by using spring forces, which were determined on the basis of clearance between the wall and the disk. Though too simplistic to properly model complex interactions between the drill string and the borehole, the model has been used as a basis for several more complex model constructions.

Tucker and Wang (1999) developed an integrated mathematical model of a drill string. Their study contained detailed equations for static configurations, boundary conditions and multiple types of force interactions between the drill string and the borehole. In a later study, Tucker and Wang (2003) developed a model based on Cosserat theory of rods. This model was used to explore two potential methods of controlling drill-string vibrations. The first controller was a simple proportional-integral controller that was used to regulate the drive speed of the system and limit stick- slip interactions between the drill string and borehole. The second controller was a torque controller, in which up-moving waves were originated at the drill bit and propagated along the drill string to attenuate the torsional vibrations of the system. Both control methods were numerically shown to be effective in limiting stick-slip oscillations of the system. The second controller was found to be the more effective of the two but it is impractical as it requires a controller to be active at the drill bit. The basis for the second controller was discussed in previous work (Tucker and Wang, 1999).

Khulief, Al-Sulaiman, and Bashmal (2007) started from a spatially continuous system to arrive at a reduced-order model of the system, made up of a set of ordinary

differential equations. These equations were then used to simulate stick-slip

interactions between the drill string and the borehole wall.

Sampaio, Piovan, and Lozano (2007) also developed a distributed-parameter

model to study coupled torsional and axial vibrations. They modeled a drill string as

initially undeformed hollow beam that undergoes axial and torsional displacements.

In order to capture the coupling between torsional and axial effects, nonlinear strain

energy equations from their previous work (Sampaio, Piovan, and Lozano, 2005)

were used to derive the equations of motion for the system. Additionally, a nonlinear

contact torque simulating the interaction between the drill bit and the bottom of the

bore well was added to the system. The predictions of the nonlinear model was

compared to that of a linear model of the system and the comparisons showed a

divergence between the predicted angular velocities of the system after the first

period of stick-slip oscillations between the drill bit and the borehole well.

A similar study was performed by Yigit and Christoforou (2006). They

included the axial movement of the drill string and new equations for the weight and

torque applied to the drill bit were developed. A linear control law was developed

after a linearization of the governing nonlinear equations of motion of the system

obtained in previous work (Yigit and Christoforou, 2000). This control law was

applied to the nonlinear system at the motor. The control scheme was shown to be

effective in reducing the vibrations of the system, providing an appropriate drive

speed could be selected for a given weight on the bit. A similar linear control was

developed by Serrarens, de Molengraft, Kok, and den Steen (1998). In this case, an

H_∞ controller was developed for the purpose of limiting sick-slip vibrations. Through

numerical efforts, this controller was shown to be useful in limiting and attenuating stick-slip vibrations in the system.

Kreuzer and Struck (2005) modeled the drill string as a long pipe with forces prescribed at the ends, the force at the top being due to the drive system of the drill string and the bottom one being due to external forces acting on the drill bit. The model allowed for axial displacement at the drill bit, but no lateral displacement and the torsional and bending vibrations were treated as being uncoupled. They started from a distributed-parameter model and reduced to a reduced-order model. By using this reduced-order model, Kreuzer and Struck showed that the torsional vibrations could be actively damped by applying a proportional-damping based controller.

Melakhessou, Berlioz, and Ferraris (2003) created a four degree-of-freedom model of a drill string. They intended to model the behavior of a drill string, when it is in contact with the borehole wall. Bending and torsional displacements were considered, and this model was used to explore the forward and backward whirling motions of the drill string.

Liao, Balachandran, Karkoub, and Abdel-Magid (2011) and Liao (2011) enhanced the work of Melakhessou, Berlioz, and Ferraris (2003) by accounting for the tilt of the drill string and stick-slip interactions between the string and borehole wall. The model of Liao *et al*. enabled more accurate simulations and helped discover dynamics not found in the work of Melakhessou, Berlioz, and Ferraris (2003). In addition, good comparisons between experimental results and model predictions were found. Vlajic, Liao, Karki, and Balachandran (2012) and Vlajic (2014) modeled the whirling motions of a drill string by using a finite degree-of-

7

freedom model. In the model development, inextensibility of the drill string was assumed, allowing the axial displacement of the string to be expressed in terms of the lateral displacements. The equations of motion were derived by using an extended Hamilton's principle and a Galerkin projection was used to obtain a reduced-order model that could capture bending and torsional motions. .

1.3 Contributions

The focus of this thesis work has been on investigating the effects of adding a secondary frequency term to the drive speed prescribed by a drill string assembly's motor. The additional term takes the form of a sinusoidal input with a chosen amplitude and frequency. A series of experimental studies have been performed to evaluate the dynamic response of the system at frequencies about and between the first lateral and torsional natural frequencies of the drill string. Following that, the equations of motion for the drill string are developed starting from the system energy components by using a distributed parameter model developed by Vlajic, Liao, Karki, and Balachandran (2012) and Vlajic (2014). Subsequently, the numerical predictions based on these equations of motion are compared with the experimental results to determine the validity of the equations of motion for the more complex system. A contribution of this thesis is a set of original experiments coupled with model simulations to examine the influence of additional frequency input additions on the dynamics of rotating, slender structures. This work could open the doors to further investigations into the use of such input additions for attenuating undesirable system motions such as whirling motions.

1.4 Organization of Thesis

In the following chapter, the setup and results for experimental studies detailing the effect of a secondary frequency on a drill string's oscillations are presented. Through these experimental efforts, additions to base drive speeds are explored when the primary drive speed is close to the natural frequencies of the first modes of torsional and bending vibrations. In the third chapter, the equations of motion for the system are presented and simulations carried out with them are discussed. The results of the simulations are compared with the experimental findings, to assess the validity of the model presented. Finally, concluding remarks are collected together and presented, along with a discussion of future avenues of research in the fourth and final chapter. References are also included. Appendix A contains details related to the development of the model. Appendix B contains the code used to analysis the video data from the experimental studies.

Chapter 2

Experimental Studies

In this chapter, the results of a series of experimental studies performed to determine the effects of the additions to the drive speed on the system dynamics are detailed. A slender aluminum rod with a rotor attached at one end is used to represent a portion of a drill-string system. The rotor has an adjustable unbalanced mass in order model the eccentricities present in a real drill string system. This string-rotor structure is driven by a servo motor at the top end of the drill string. The complete experimental arrangement is depicted in Figure 2.1. In this unique laboratory scale arrangement, the flexible structure dimensions have been chosen so that the relative locations of the first bending and torsion frequencies have similar characteristics as in a full scale drill string.

The servo motor is programed to apply a drive speed of the form $\dot{\beta} = \Omega + \alpha cos(\omega t)$ where Ω is the base drive speed, ω is the secondary frequency, and α is the amplitude of the secondary frequency input. Video footage of the system's response to the drive speed input was recorded by using a digital camera and processed to determine the amplitude response of the system. Data were taken for base drive speeds approaching the respective natural frequencies of the first bending and first torsional modes of the system and for secondary frequencies ranging from 0.25 Hz to 5.0 Hz.

Figure 2.1. Experimental arrangement used to study the dynamics of a drill-string section. The rotor is at the bottom and a chuck is used at the top.

2.1 Design and Setup

The experimental model for the drill string consisted of three components: i) a rotor with an attached unbalanced mass, ii) a slender rod, hereafter referred to as a string, and iii) a servo motor. The rotor consisted of an aluminum disk attached to a chuck through a slender aluminum string which was attached to the disk's center.

This rotor-string assembly is presented in Figure 2.2. The rotor had a set of holes drilled through it that extended radially from its center to its edge. This allowed the eccentricity of the unbalanced mass with respect to the rotor's center of mass to be varied. The unbalanced mass consisted of a set of nuts and bolts that could be securely fastened through the holes in the disk. The holes were threaded so as to securely hold the bolt in place and prevent the unbalanced mass from rattling during the experiments. The weight of the unbalanced mass could be varied by changing the number of nuts secured to the bolt. This configuration can be seen in Figure 2.3. The rotor-string assembly is attached to a chuck at the other end of the string. This chuck is in turn connected to the drive shaft of the servo motor, allowing the string-rotor assembly to be driven at different speeds by the motor. The driveshaft and motor assembly is shown in Figure 2.4.

Figure 2.2. Rotor-string assembly used in the experiments.

(a)   (b)
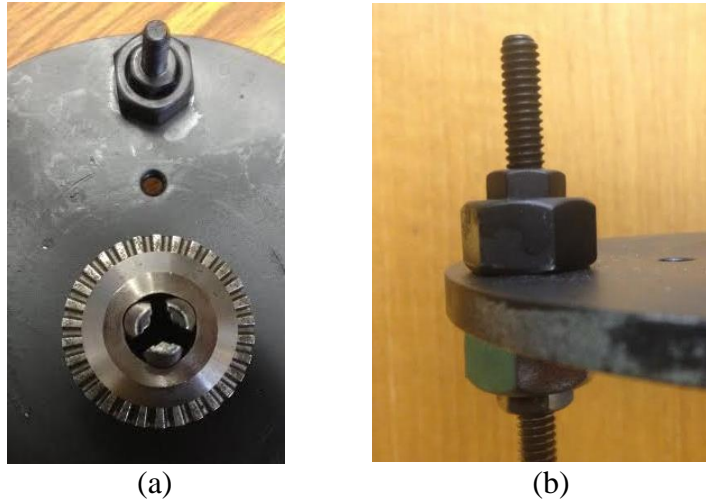
Figure 2.3. Configuration of the unbalanced mass: (a) top-down view of the holes used to vary the eccentricity and (b) the nuts and bolt that made up the unbalanced mass.

Figure 2.4. Motor assembly used in the experiments.

A high-speed digital camera placed near the chuck, as shown in Figure 2.4, was used to track the amplitudes of lateral oscillations of the drill string. In order to use the imaging system to track the lateral displacements of the rotor-string assembly

while the system is in operation, a section of the string connected to the rotor was wrapped in white tape and a thin shell of black paper was constructed around the tape. Additionally, the rotor was spray-painted black and a backdrop made with the same black paper was used to prevent the imaging system from tracking light reflecting off the rotor due to background events. This setup is depicted in Figure 2.5. The camera was set to record data in monochrome and its aperture stop was made small to darken the image, allowing for greater contrast between the white tape and black background and making it easier to use the image processing software for tracking the displacement.

Data were collected for a set of base drive speeds near the first torsional and bending natural frequencies, with secondary frequencies beginning at 0.5π radians/sec and ranging upward. When collecting data for a chosen combination of drive speed

Figure 2.5. White tape and paper shell used to help track lateral displacements.

14

and secondary frequency, at least two minutes duration was allowed for the system to reach a steady-state response. Video of the steady-state system response was then recorded for forty to fifty seconds at fifty frames per second. Additionally, before each set of tests, a photograph was taken of the system at rest. This photograph was used to determine the location of the equilibrium position of the model.

After the data were collected, it was run through image processing code in Matlab. The program was used to further enhance the contrast between the white section of the drill string and the black backdrop. The program was used to go through the footage frame by frame tracking the position of white section of the drill string. These points were then compared to the position of the equilibrium point of the system to determine the amplitude response of the system.

When collecting data, secondary frequencies below 0.5π radians/sec were avoided, as the program controlling the servo motor was found to experience memory errors if the secondary frequency was dropped below that threshold. First, data would be taken for the system response at a base drive speed without a secondary frequency as a baseline. After that, a secondary frequency was added to the drive speed. Starting at 0.5π radians/sec, the secondary frequency was increased in 0.25π radians/sec increments with the response data being recorded at each new secondary frequency. This increase continued until the servo motor was unable to provide the required secondary frequency due to vibrations in the system.

The system parameters for the experimental model are listed below in Table 2.1. The values for the natural frequencies and damping ratios were determined

experimentally by tracking the system displacement responses and applying the logarithmic decrement equations to the results. The bending frequency and associated damping ratio were determined by applying a lateral displacement to the system and tracking the response of the system. The process was similar for determining the torsional frequency and damping ratio, with an angular initial displacement applied to the system rather than a lateral displacement. In order to track the angular oscillation, white tape was placed on the unbalanced mass as well as the string. By using these two points of reference, the angular oscillation was tracked.

Table 2.1. Experimental system parameters.

Parameter	Value	Units
d_r	0.2651	m
d_{chuck}	0.03	m
$d_{connect}$	.0508	m
h_r	0.0127	m
h_{chuck}	0.03	m
$h_{connect}$	0.0127	m
L	0.857	m
r	0.00238	m
e	0.0635	m
m	0.0617	kg
M	0.970	kg
E	$70*10^9$	Pa
G	$25*10^9$	Pa
$\omega_{n,b}$	1.52π	rad/s
$\omega_{n,t}$	8.2π	rad/s
ζ_b	0.00087	
ζ_t	0.011	

2.2 Results for Drive Speeds around the First Bending Natural Frequency

The first bending natural frequency for the string-rotor assembly is 1.52π rad/s (0.76 Hz or ~46 RPM). Hence, data were collected for base driving speeds at π rad/s (30 RPM) and 1.33π rad/s (40 RPM). This was done to observe the effects of secondary frequency on the system as the drive speeds approached the first bending frequency. The system was not driven at a base drive speed at the aforementioned natural frequency in order to avoid driving the system at resonance, a condition which could potentially damage the system.

When the system was driven at a base drive speed of π rad/s, the servo motor was able to sustain the range of secondary frequencies from 0.5π rad/s to 8.75π rad/s. The amplitude response of the system across this range is shown in Figure 2.6. For secondary frequencies at the low end of this range, the amplitude response of the system is observed to increase greatly. As the speed of the secondary frequency is increased, the response amplitude of the system was found to decrease, eventually, dropping below the response amplitude of the system in the absence of a secondary frequency input. This attenuation in the amplitude was found to continue until the secondary frequency approached 4.75π rad/s, at which point the response amplitude increased above the base system response amplitude. Subsequently, the amplitude response was found to be attenuated once more as the secondary frequency was increased beyond 4.75π rad/s and the system response remained this way through the rest of the experiments.
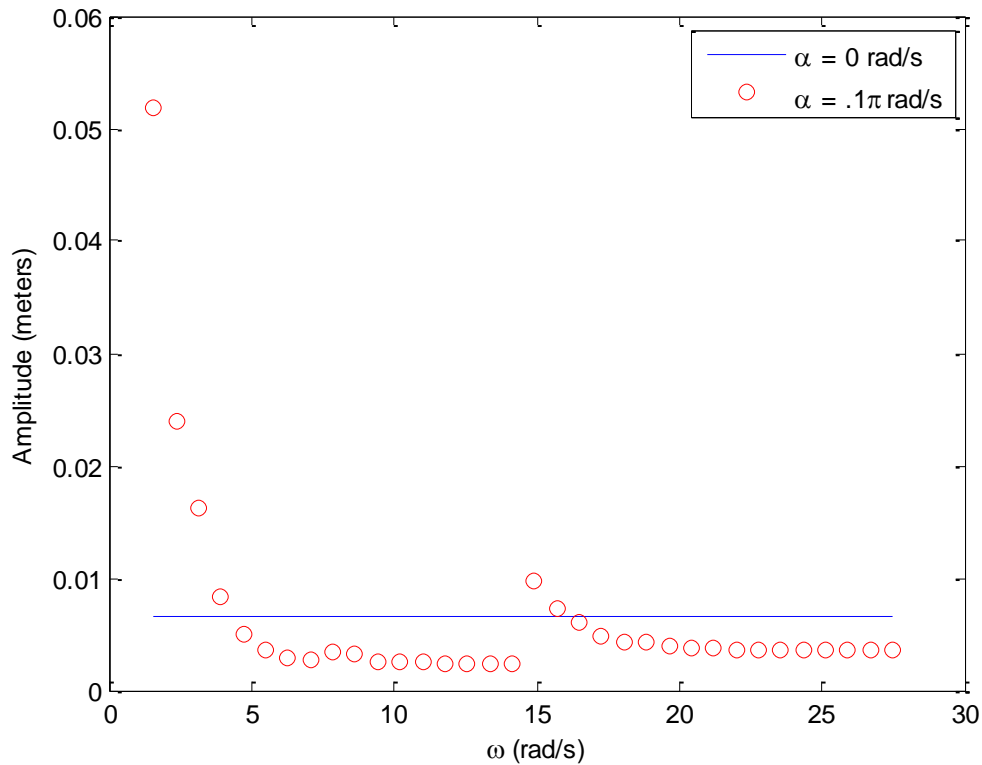
Figure 2.6. Amplitude response for system at base drive speed of π rad/s.

When the system was driven at a base drive speed of 1.33π rad/s, the servo motor was able to sustain the range of secondary frequencies from 0.5π rad/s to 8.75π rad/s. The resulting amplitude response of the system observed across this range is shown in Figure 2.7. For secondary frequencies at low end of this range, the response amplitude of the system was found to increase slightly above the case without the secondary frequency addition. As the speed of the secondary frequency is increased, the system amplitude response rapidly decreased, barely dropping below the response of the system without a secondary frequency input. From then on, the attenuation of the system remained very small and almost constant for the range of considered secondary frequency inputs.
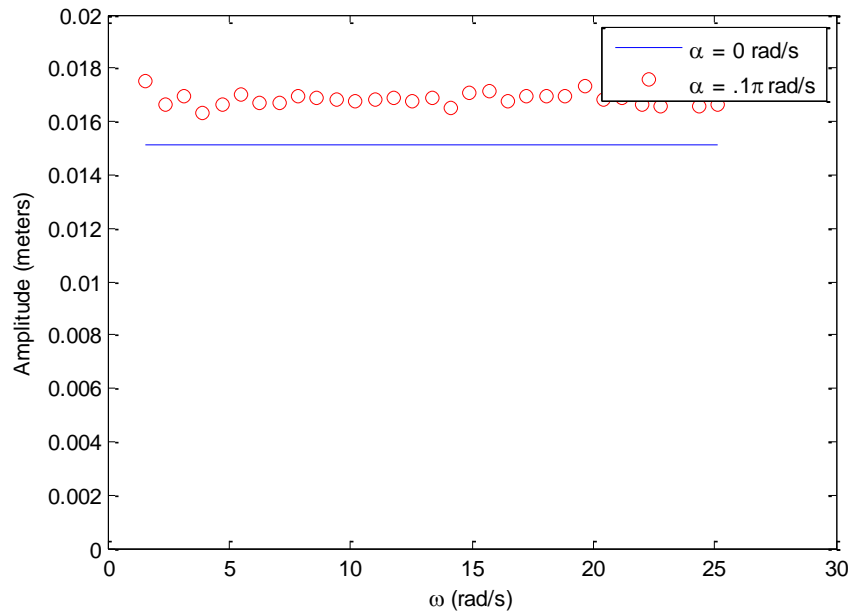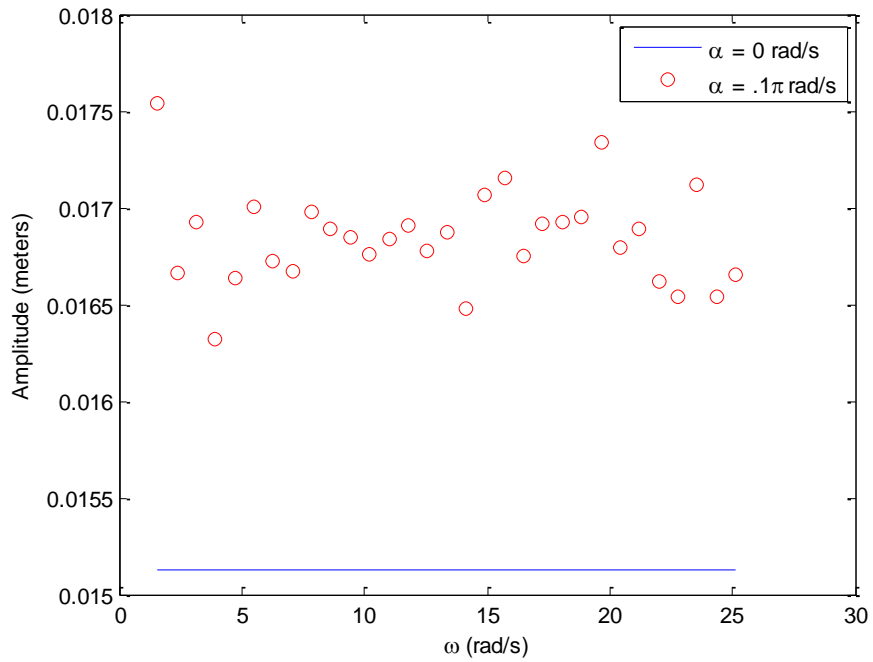
Figure 2.7. (a) Amplitude response for system at base drive speed of 1.33π rad/s. (b)

Expanded view.

19

2.3 Results for Drive Speeds around the First Torsional Natural Frequency

The first torsional natural frequency for the system is significantly higher than that of the first bending natural frequency, being, about 8.2π rad/s (4.1 Hz or 246 RPM). Data were collected for base driving speeds of 7.67π rad/s (~230 RPM) and 8π rad/s (240 RPM). This was done to observe the effects of secondary frequency addition on the system response, as the drive speed approached the first torsional frequency. As was the case for primary drive speeds close to the lateral natural frequency, the system was not driven at a base drive speed at the aforementioned natural frequency to avoid a resonance situation, which could be potentially harmful to the system.

When the system was driven at a base drive speed of 7.67π rad/s, the servo
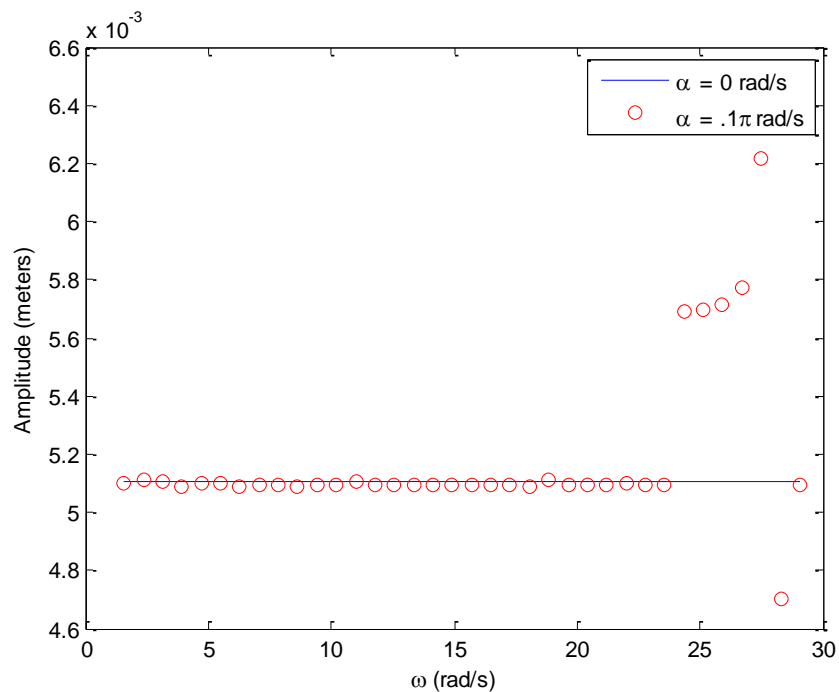
Figure 2.8. Amplitude response for system at base drive speed of 7.67π rad/s.
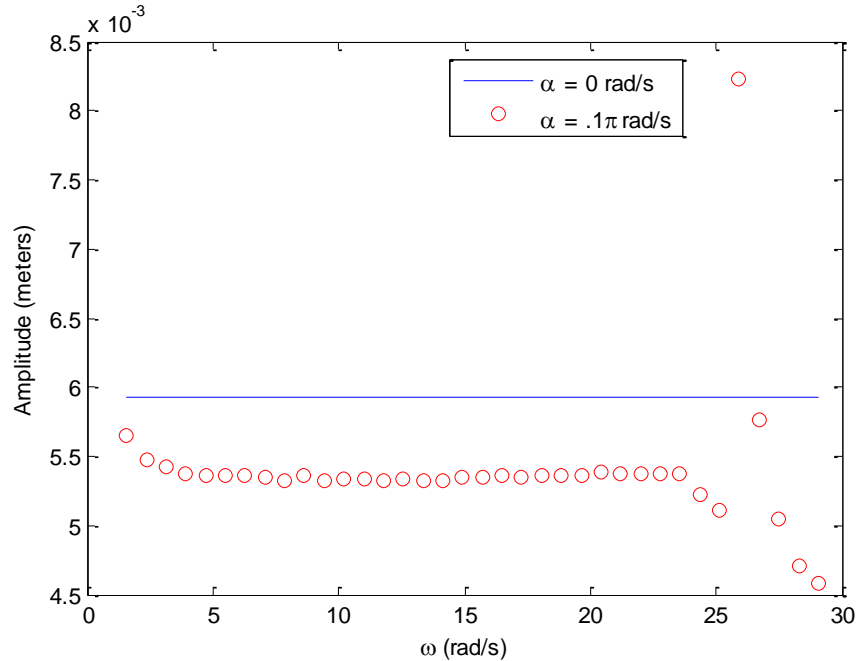
Figure 2.9. Amplitude response for system at base drive speed of 8π rad/s.

motor was able to sustain the range of secondary frequencies from 0.5π rad/s to 9π rad/s. The amplitude response of the system across this range is shown in Figure 2.8. For most of the secondary frequency inputs, there is not much attenuation in the system response amplitude when compared with the system response without a secondary frequency. This exception to this is at 8.5π rad/s were the system experiences a moderate amplification in the system response. This amplification is found to rapidly attenuate as the secondary frequency is increased past 8.5π rad/s.

When the system was driven at a base drive speed of 8π rad/s, the servo motor was able to sustain the range of secondary frequencies from 0.5π rad/s to 9.25π rad/s. The amplitude response of the system across this range is shown in Figure 2.9. The overall system response to the secondary frequencies is seen to show some attenuation. An amplification is seen in the system response around 8.5π rad/s, as

21

seen in the previous set of experiments associated with the base drive speed case of

7.67π rad/s. Additional experimental results are included in Chapter 3, wherein

comparisons between numerical results and experimental predictions are provided.

When attenuation is observed in the system response due to the addition of a

secondary-frequency input, it is suspected that the addition of a new frequency input

steers the system to a different response region.

Chapter 3: Numerical Studies and Comparisons between Numerical and Experimental Results

In this chapter, a model for the drill sting is adapted from previous work (Vlajic *et al*. 2012) to assess the addition of secondary-frequency inputs and the simulation results are compared to experimental results from the previous chapter. The equations of motion used for the model are a reduced-order system obtained through a Galerkin projection from a distributed parameter system obtained by using the extended Hamilton's principle. The reduction is carried out by considering projections based on the first torsional and bending modes of the system. A force interaction model representing interactions between the rotor-string system and a stator is also presented. The reduced system is numerically solved for different base drive speeds corresponding to those used in the experimental studies. The range of secondary frequencies considered in the simulations is larger than that considered in the experiments. The numerical results are compared to the experimental results. Finally, a preliminary study conducted on the effects of the secondary frequency additions in the presence of borehole interactions is also presented.

3.1 Equations of Motion for the String-Rotor Model

The model development for this thesis work follows earlier work from the author's research group (Vlajic, Liao, Karki, and Balachandran, 2012 and Vlajic, 2014). The kinetic energy of the drill string running from $x = 0$ to $x = $ L, rotor, and the unbalanced mass of the string-rotor system located at $x = L$ can be written as follows:

$$T_{string} = \int_0^L \left[\rho A(\dot{u}^2 + \dot{v}^2 + \dot{w}^2) + \rho I(\dot{v}'^2 + \dot{w}'^2) + \rho I_o \dot{\beta}^2 \right.$$
$$\left. + 2\rho I_o \dot{\beta} \dot{v}' w' \right] dx \quad (3.1)$$

$$T_{rotor} = \frac{1}{2} \left[M(\dot{u}^2 + \dot{v}^2 + \dot{w}^2) + I_D(\dot{v}'^2 + \dot{w}'^2) + I_{Do}(\dot{\beta}^2 + 2\dot{\beta}\dot{v}'w') \right]|x = L \quad (3.2)$$

$$T_{mass} = \frac{m}{2} \left[\dot{u}^2 + \left(\dot{v} - \dot{\beta}e\sin(\beta)\right)^2 + \left(\dot{w} + \dot{\beta}e\cos(\beta)\right)^2 \right]|x = L \quad (3.3)$$

In these equations, $u = u(x, t)$, $v = v(x, t)$, and $w = w(x, t)$ are the axial and lateral displacement fields, respectively, and the partial derivatives with respect to x and t are indicated by the operations $(\dot{\cdot})$ and $(\cdot)'$, respectively. The variable x is defined such that $x=0$ represents the end of the drill string that is connected to the motor assembly and $x=L$ is at the end attached to the rotor and unbalanced mass. The rotational motion prescribed by the motor at $x=0$ is of the form $\Omega + \alpha\cos(\omega t)$, where Ω is a constant drive speed, ω is a secondary frequency, and α is the amplitude of the secondary frequency. From this, the term $\beta(t)$ can be derived as $\beta(t) = \Omega t + \frac{\alpha}{\omega}\sin(\omega t) + \theta(x, t)$, where $\theta(x, t)$ is the angular deformation of the system.

Assuming that the system is linearly elastic, the potential energy of the string-rotor system can be developed as

$$U = \frac{1}{2} \int_0^L \left[EAu'^2 + EI(v''^2 + w''^2) + GI_o\beta'^2 - 2Mgu' \right] dx \quad (3.4)$$

and the virtual work done on the system due to contact with the stator is given by

$$\delta W = \lambda \left(\frac{F_{fr}d_r}{2} \delta\beta + F_v \delta v + F_w \delta w \right) \quad (3.5)$$

24

The quantities M, I_D, and I_{Do} in Eq. (3.2) are derived below. The rotor and the chuck that connect it to the string are treated a system consisting of three discs. The chuck is treated as two discs to account for the fact that it has both steel and aluminum components.

$$m_{chuck,steel} = \frac{\rho_{steel} h_{chuck} \pi d_{chuck}^2}{4} \quad (3.6)$$

$$m_{chuck,Al} = \frac{\rho_{Al} h_{connect} \pi d_{connect}^2}{4} \quad (3.7)$$

$$m_{rotor} = \frac{\rho_{steel} h_r \pi d_r^2}{4} \quad (3.8)$$

$$M = m_{chuck,steel} + m_{chuck,Al} + m_{rotor} \quad (3.9)$$

$$I_D = \frac{m_{chuck,steel}(3d_{chuck}^2 + 4h_{chuck}^2) + m_{chuck,Al}(3d_{connect}^2 + 4h_{connect}^2)}{48}$$

$$+ \frac{m_{rotor}(3d_r^2 + 4h_r^2)}{48} \quad (3.10)$$

$$I_{Do} = \frac{m_{chuck,steel} d_{chuck}^2 + m_{chuck,Al} d_{connect}^2 + m_{rotor} d_r^2}{8} \quad (3.11)$$

Eqs. (3.1) - (3.5) are used as a starting point, and the following assumptions and approach are used to derive the governing equations of motion for the rotor-string system. Due to the physical constraints and geometry of the system, the axial displacement of the string, $u(x,t)$, is related to the lateral displacements, $v = v(x,t)$ and $w = w(x,t)$; that is,

$$u' = \frac{1}{2}(v'^2 + w'^2) \quad (3.12)$$

Since the axial vibratory modes of the system have much higher natural frequencies compared to those of the torsional and lateral modes, axial vibrations are

not considered here. The mass of the drill sting is very small compared to the mass of the rotor and this mass is also neglected. The spatial and temporal parts of the lateral and torsional displacements are assumed to be able to be separated into the following forms:

$$v(x,t) = \sum_{i=0}^{N} V_i(t)\phi_{v,i}(x) \quad (3.13)$$

$$w(x,t) = \sum_{i=0}^{N} W_i(t)\phi_{w,i}(x) \quad (3.14)$$

$$\theta(x,t) = \sum_{i=0}^{N} \Theta_i(t)\phi_{\theta,i}(x) \quad (3.15)$$

The extended Hamilton's Principle is used to derive the partial differential equations of motion with the associated boundary conditions. Subsequently, Galerkin's method is then used to cast the system of partial differential equations into a system of three coupled ordinary differential equations corresponding to the bending motions in the two directions and the torsion motion. This reduction has been carried out under that the assumption that only the first bending and torsion modes dominate the system response. The justification for a single mode assumption along each of the two bending directions and the torsion direction is based on the experimental arrangement discussed in the last chapter. The governing equations of motion are given by Eqs. (3.16) - (3.18), and the associated coefficients can be found in Appendix A. A more detailed derivation can be found in the work of Vlajic (2014). All terms containing β are determined at x = L.

$$a_1 \ddot{V} + a_2 \dot{V} + a_3 \Omega \dot{W} + a_4 V + a_5 \left(\dot{\Theta} \dot{W} + \ddot{\Theta} W \right) - me\phi_v \phi_\theta \ddot{\Theta} \sin(\beta)$$

$$- me\phi_v \dot{\beta}^2 \cos(\beta) = \lambda F_v \quad (3.16)$$

$$b_1 \ddot{W} + b_2 \dot{W} + b_3 \Omega \dot{V} + b_4 W + b_5 \dot{\Theta} \dot{V} + me\phi_w \phi_\theta \ddot{\Theta} \cos(\beta)$$

$$- me\phi_w \dot{\beta}^2 \sin(\beta) = \lambda F_w \quad (3.17)$$

$$c_1 \ddot{\Theta} + c_2 \dot{\Theta} + c_3 \Theta + c_4 \left(\ddot{V} W + \dot{V} \dot{W} \right) + me \ddot{W} \phi_w \phi_\theta \cos(\beta)$$

$$- me \ddot{V} \phi_v \phi_\theta \sin(\beta) = \lambda F_{fr} \frac{d_r}{2} \quad (3.18)$$

Here, λ is defined as

$$\lambda = \begin{cases} 0 \ for \ R < \delta \\ 1 \ for \ R \geq \delta \end{cases} \quad (3.19)$$

where δ indicates the clearance between the rotor and the stator while the system is at rest and R is amplitude of the rotor's oscillations, defined by the equation

$$R = \sqrt{w(L,t)^2 + v(L,t)^2} \quad (3.20)$$

3.2 Force-Interaction Model

The force interaction model used for this system has been adapted from work by Vlajic (2014) and this model is designed to account for changes in the friction coefficient as the system transitions between slipping and sticking motions. The normal force generated by the contact between the rotor and the stator is assumed to be linearly proportional to the deformations of the stator, as the stator itself is made from a linear elastic material. From the considered parameters, the equations for the frictional and normal forces can be derived as

$$F_N = \begin{cases} 0 & for \ R \leq \delta \\ K(R - \delta) \ for \ R > \delta \end{cases} \quad (3.21)$$

$$\mu = -\frac{2}{\pi} \tan^{-1}(\epsilon_f v_{rel}) \left[\frac{\mu_s - \mu_k}{1 + \delta_f |v_{rel}|} + \mu_k \right] \quad (3.22)$$

$$F_{fr} = \mu * F_N \quad (3.23)$$

The frictional force will oppose the motion and have the opposite sign of the

relative velocity between the two surfaces generating the friction. Unfortunately,

signum functions are not continuous and they are difficult to utilize in numerical

integration methods. Hence, the signum function that would normally be used in Eq.

(3.22) has been replaced with an inverse tangent function in order to give a smooth

approximation for the friction force. The quantity ϵ_f determines how steep the

approximation is and consequentially how accurate the representation is. The δ_f term

in Eq. (3.22) is a positive constant that represent the rate at which the static

coefficient of friction transitions to the kinetic coefficient of friction with respect to

the relative velocity between the rotor and the stator.

In order to relate the normal and tangential forces back to Eqs. (3.16) – (3.18),

they were transformed to accommodate the expressions for external work in the

equations of motion. This is accomplished by relating them back to the directional

forces Fv and Fw, resulting in the equations

$$F_v = \frac{-F_{fr}W - F_N V}{R} \quad (3.24)$$

$$F_w = \frac{F_{fr}V - F_N W}{R} \quad (3.25)$$

3.3 Numerical Studies

The structural equation for the string-rotor system given by Eqs. (3.13) –

(3.15) were numerically solved by using a second-order Rosenbrock integration

scheme. The absolute and relative tolerances were set to 1e^{-6}. The parameters for the

simulations are provided in Table 2.1. A time scale of 1000 seconds was simulated

for each set of base drive speeds and secondary frequencies to allow for the system to

reach a steady-state response. The amplitude response was calculated based on the

last twenty seconds of data. As in the experimental studies, the system response to

the base drive speed without a secondary frequency input was first simulated and the

secondary frequency input was added in subsequent tests. Due to the simulations not

having the same limitations as the experimental system, a wider range of secondary

frequencies could be studied in the simulations. The secondary frequency value was

started from 0.25π rad/s and this value was increased by 0.25π rad/s after each test, up

to a maximum to 20π rad/s. The initial displacements of the system were assumed to

be zero for the test involving the only the base drive speed. The subsequent

simulations with the secondary frequency inputs assumed initial conditions

corresponding to the response for a previous secondary frequency input.

3.4 Simulations for Drive Speeds around the First Bending Natural Frequency

The first bending natural frequency for the string-rotor assembly was

estimated by the code to be 1.488π rad/s (~45 RPM). Like the experimental study,

data was collected for base driving speeds between at π and 1.33π rad/s. The

amplitude secondary frequency in the simulation remains the same as in the

experimental study, with a value of 0.1π rad/s.

The response for the system at a base drive speed of π rad/s is shown in Fig 3.1. When the system was driven at a base drive speed of π rad/s, the amplitude response of the system was greatly amplified for low speed secondary frequencies with a large amplification occurring at 0.5π rad/s. As the speed of the secondary frequency increased beyond 0.5π rad/s, the amplitude response of the system rapidly decayed, dropping back to the same amplitude response as the system without a secondary frequency at 0.75π rad/s. The system has another small amplification at 2.5π rad/s, at which point the amplitude increases above the base system again. The amplitude response then attenuates once more as the secondary frequency increases to 2.75π rad/s, dropping back to the baseline response system and remaining this way for the rest of the observable data.

When the system is driven at π rad/s with no secondary frequency, the amplitude response of the drill string is fairly constant and circular as depicted below in Figure 3.2. At steady state, the system response prescribes an almost perfect circle with a radius of 0.003 meters. As the secondary frequency is added to the drive speed, the amplitude response of the system increases drastically, reaching a peak when the secondary frequency is 0.5π rad/s. The consistent circular response of the system began to decay, developing the period-three circular lobe shape displayed in Figure 3.3.
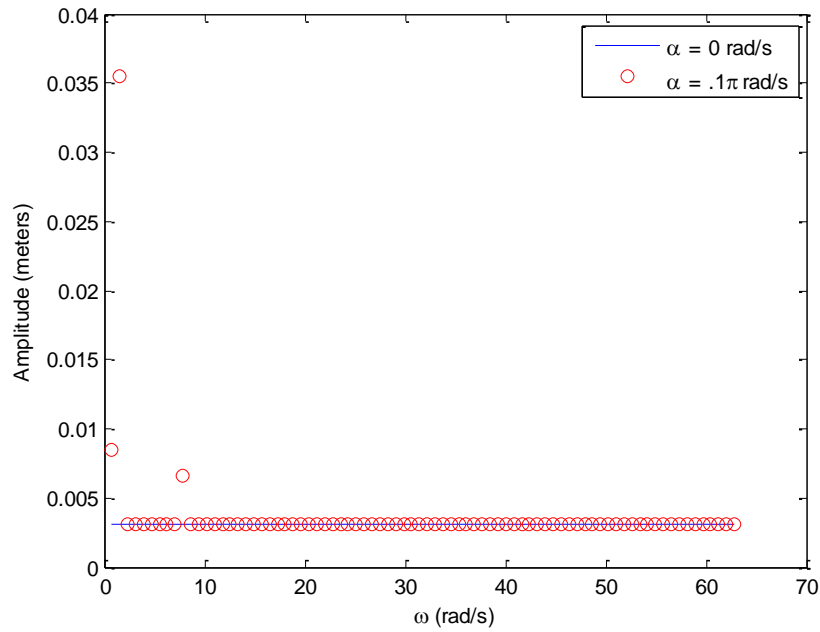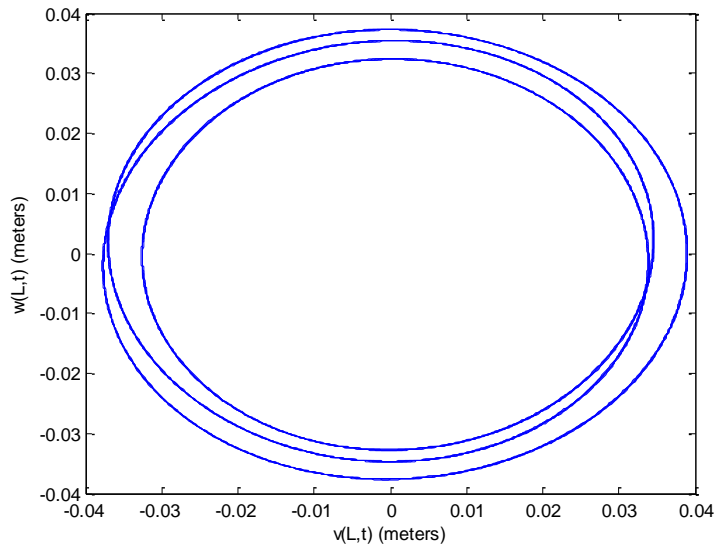
Figure 3.1. Amplitude response of drill string at base drive speed of π rad/s.
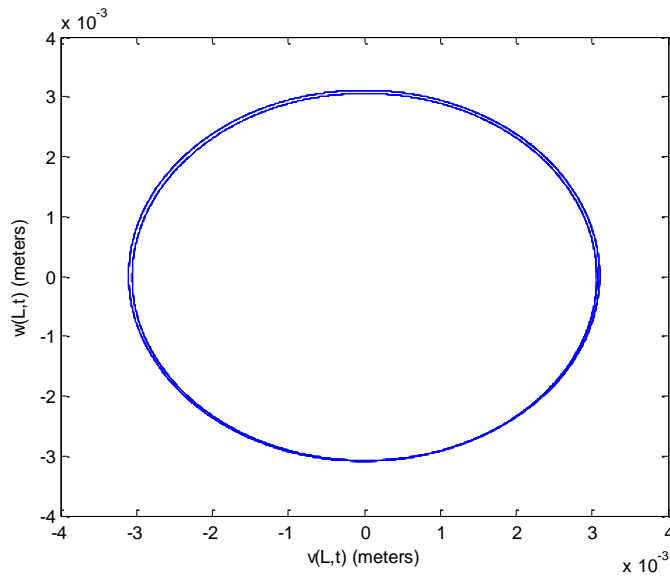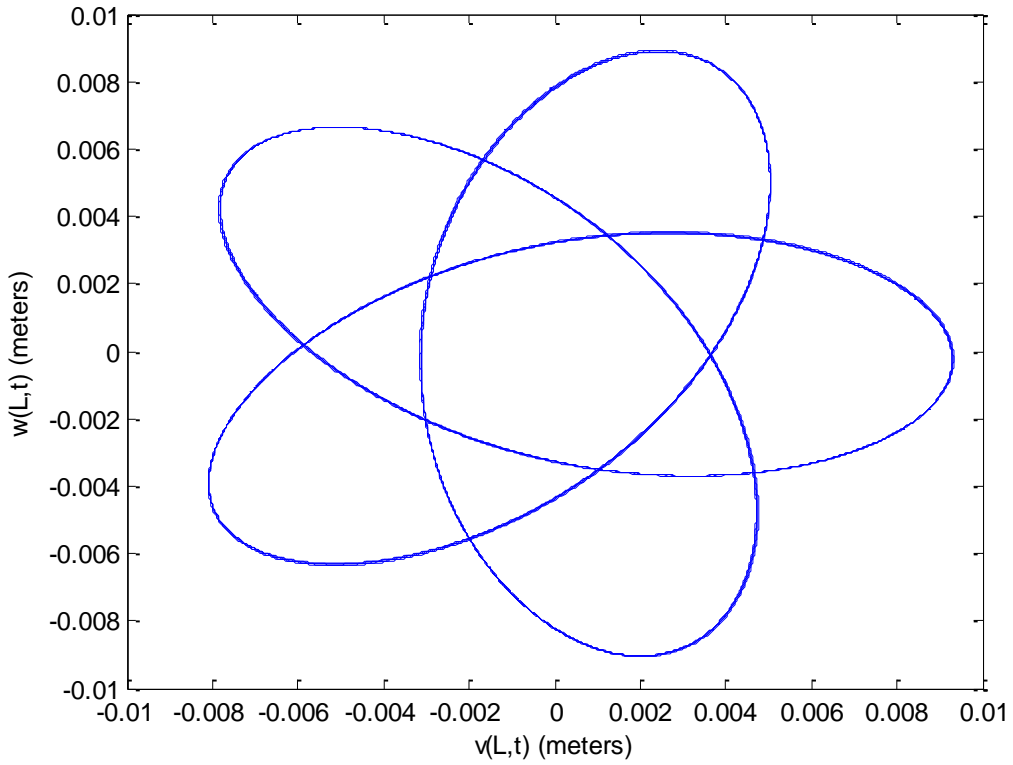

Figure 3.2. Displacement response of drill string when driven at π rad/s with no
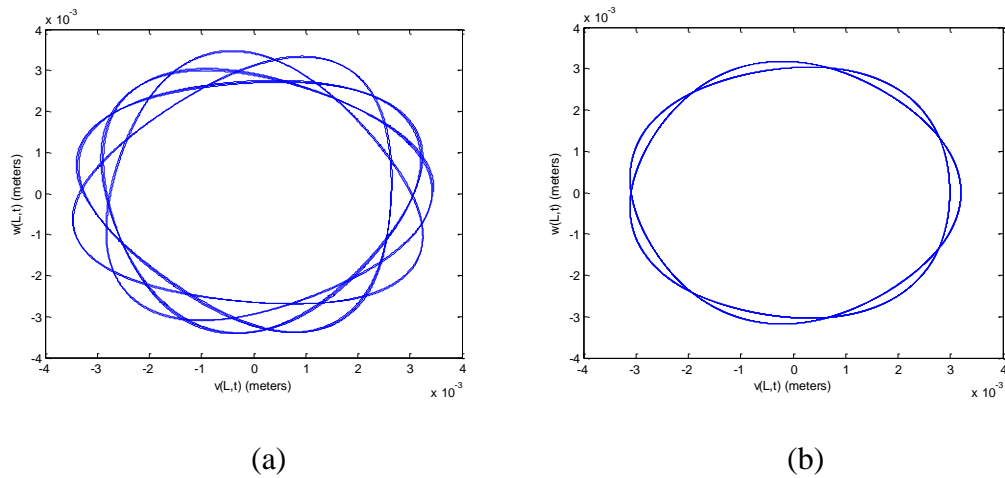
secondary frequency addition.

Figure 3.3. Displacement response of drill string when driven at a primary speed of π

rad/s with a secondary frequency addition of 0.5π rad/s.

As the secondary frequency increased beyond 0.5π rad/s, the amplitude

response of the system rapidly decayed back to baseline response of the system.

Though the amplitude of the response remained constant as the secondary frequency

increased the lobe shape of the system continued to become less circular. This

eventually resulted in a small amplification of the amplitude response at 2.5π rad/s,

were the lope shape of the amplitude response took on a star-shaped pattern, as shown

in Figure 3.4. As the frequency continued to increase, the amplitude response once

again decreased back to baseline response, both in terms of the amplitude and the

lobe shape. This process is depicted in Figure 3.5.
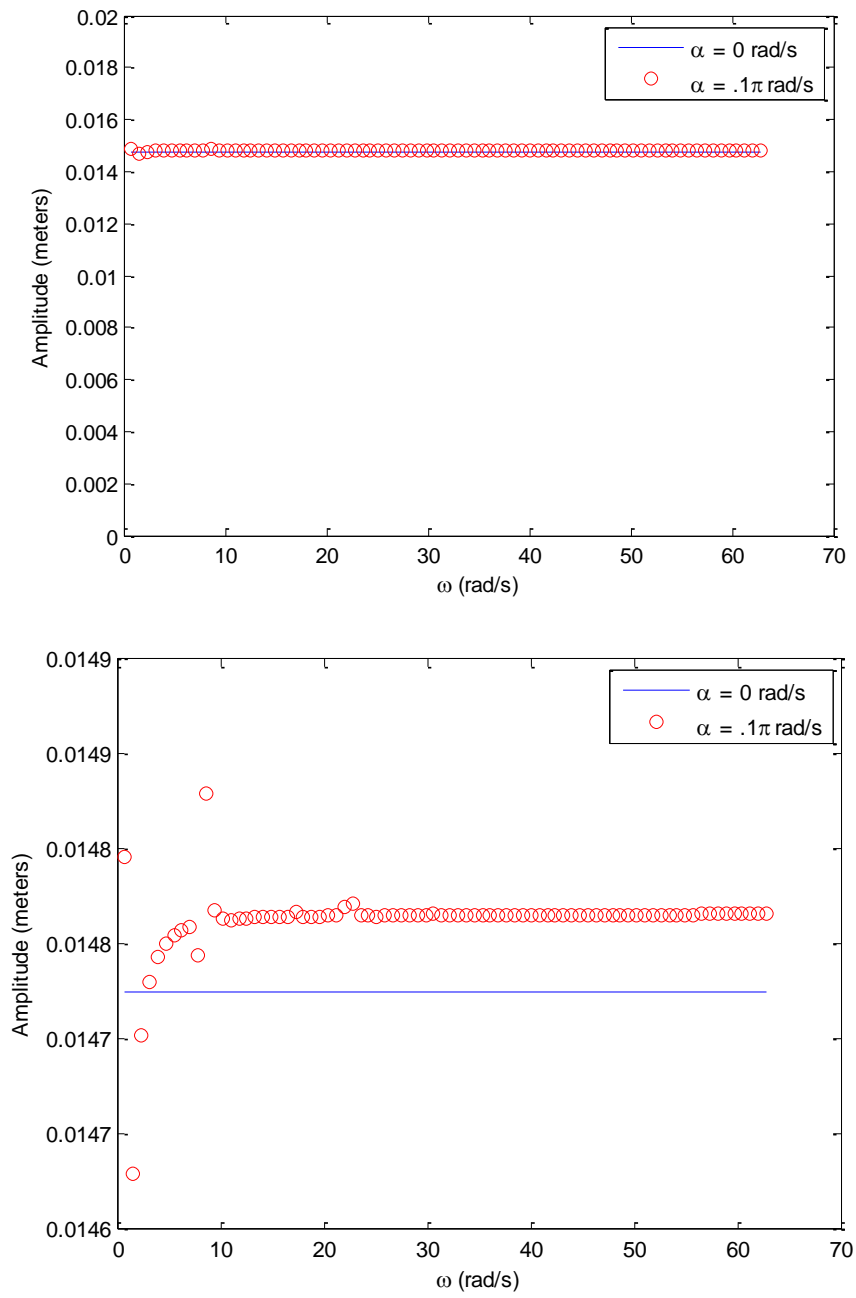
Figure 3.4. Displacement response of drill string when driven at a primary speed of π

rad/s with a secondary frequency addition of 2.5π rad/s.
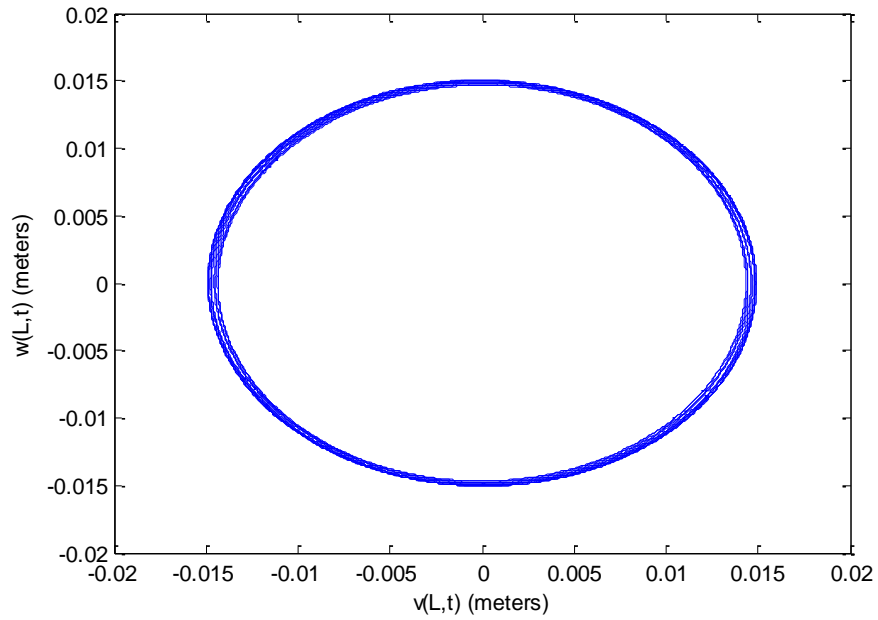

(a)   (b)

Figure 3.5. Displacement response of drill string when driven at a primary speed of π

rad/s with a secondary frequency addition: (a) 2.75π rad/s and (b) 3.5π rad/s.

The response for the system at a base drive speed of 1.33π rad/s is shown in

Figure 3.6. When the system was driven at a base drive speed of 1.33π rad/s, the

addition of q secondary frequency to the drive signal had almost no effect on the

response of the system. Over the range of secondary frequencies from 0.25 – 10.00

Hz there is less than a 1% shift in the amplitude response, with slight attenuation at

lower secondary frequencies and slight amplification at the higher frequencies. The

lobe shape of the amplitude response for the baseline system is fairly constant though

somewhat more varied than the baseline response of the system driven at π rad/s.

Once the secondary frequency is added in, the lobe shape of the response becomes

slightly more varied for lower speed secondary frequencies. As the secondary

frequency of the system continues to increase, the lobe shape of the system response

began to collapse back to the lobe shape prescribed by the baseline response. Though

there is a slight amplification at higher speed secondary frequencies it is almost

negligible and there is no noticeable change in the lobe shapes of the amplitude

response at these higher frequencies. The progression of the lobe shape of the

amplitude response as the secondary frequency increases is detailed in Figures 3.7 –

3.9.

Figure 3.6. Amplitude response of drill string driven at 1.33π rad/s (top). Expanded view of amplitude response (bottom).

Figure 3.7. Displacement response of drill string when driven at a primary speed of

1.33π rad/s with no secondary frequency addition.
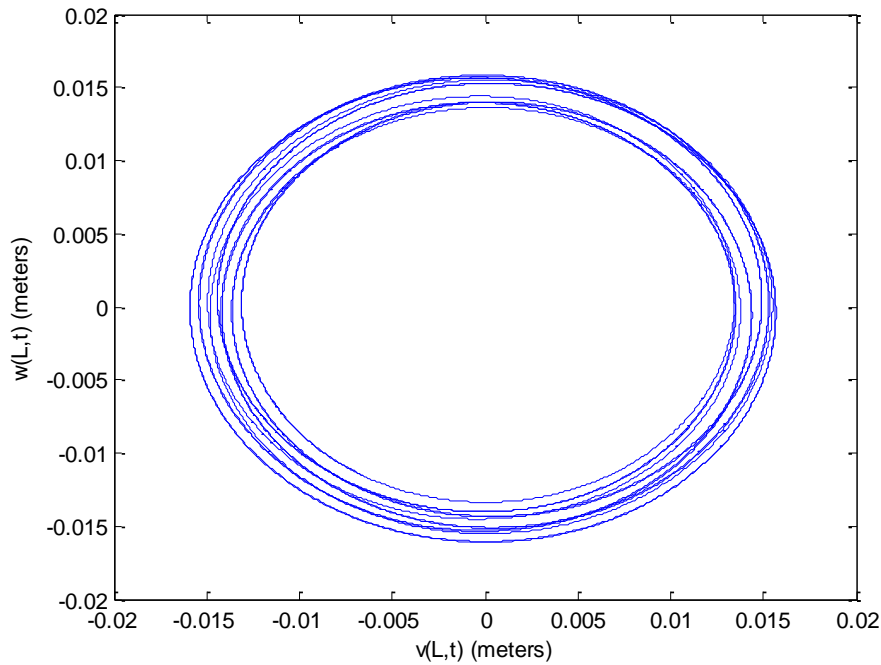
Figure 3.8. Displacement response of drill string when driven at a primary speed of

1.33π rad/s with a secondary frequency addition of 0.5π rad/s.

36
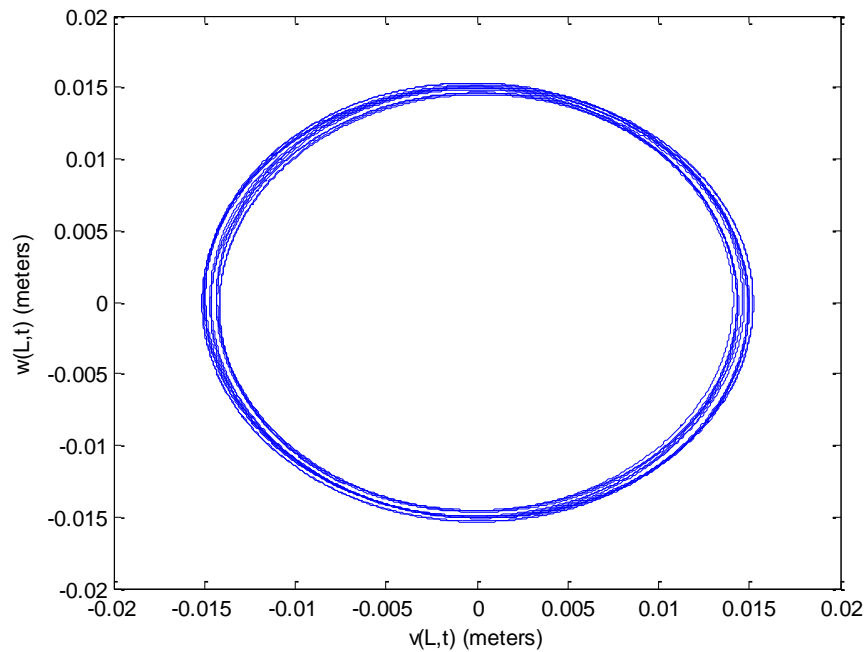
Figure 3.9. Displacement response of drill string when driven at a primary speed of 1.33π rad/s with a secondary frequency addition of 2π rad/s.

3.5 Simulations for Drive Speeds around the First Torsional Natural Frequency

The first torsional natural frequency estimated by the simulation was significantly higher than that of the bending frequency, being about 7.4π rad/s (~222 RPM) Data was collected for base driving speeds of 7.67π and 8π rad/s. The amplitude of the secondary frequency remained the same as the previous tests.

The response for the system at a base drive speed of 7.67π rad/s is shown in Figure 3.10. When the system was driven at a base drive speed of 7.67π rad/s, the amplitude response of the system remained largely unaffected by the addition of a
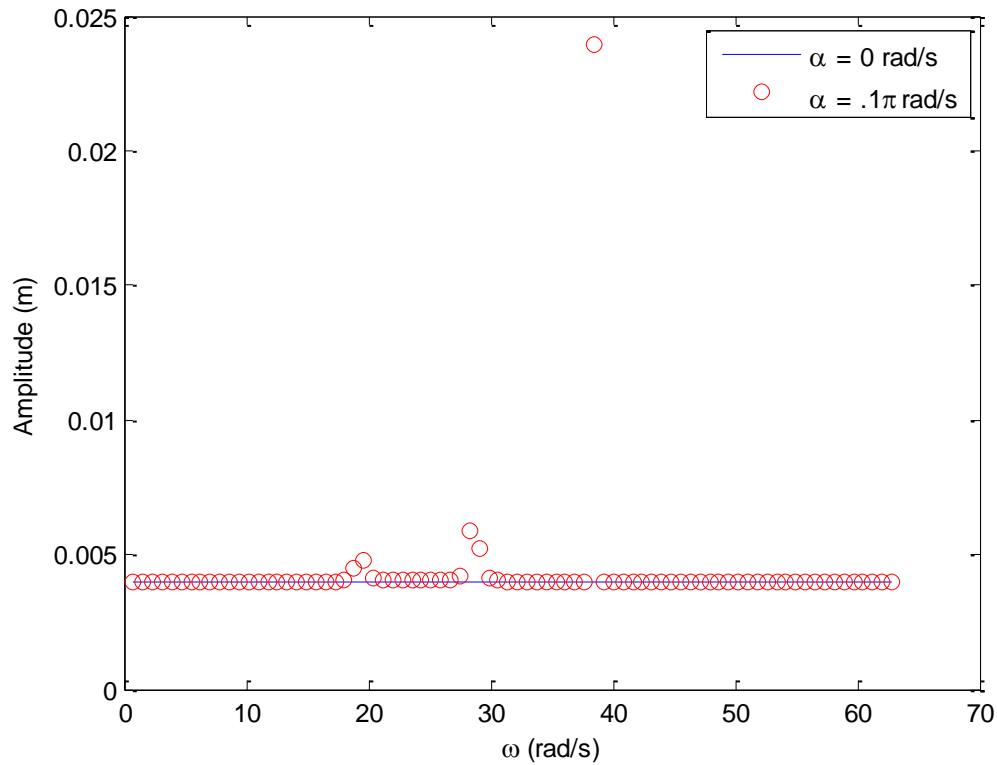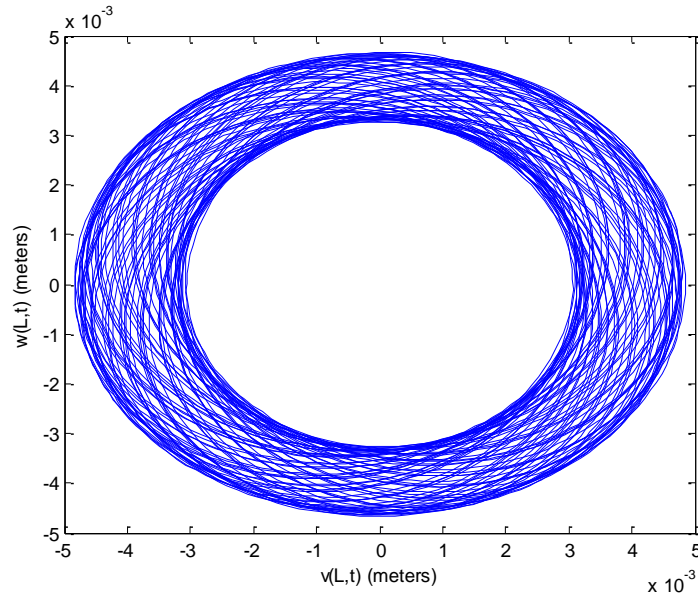
Figure 3.10. Amplitude response of drill string at base drive speed of 7.67π rad/s.

secondary frequency. The exceptions to this were the secondary frequencies around 6π, 9π and 12π rad/s where large amplifications in the amplitude occurred, with each amplification being larger than the last. Interestingly, the frequencies at which the amplifications occur do not correspond to any of the natural frequencies of the system.

The amplitude response of the simulation for a drill string driven at 7.67π rad/s prescribed a circular response that was similar in shape to those of the system when driven at π and 1.33π rad/s but with more variation in the amplitude than the previous cases. This response is shown in Figure 3.11. The addition of the secondary frequency did little to alter the amplitude and shape of the amplitude response of the

38

Figure 3.11. Displacement response of drill string when driven at a primary speed of

7.67rad/s with no secondary frequency addition.

system until the secondary frequency approached 6π, 9π, 12π. As depicted in Figures

3.12 – 3.15, as the secondary frequency approached 6π rad/s the lobe shape of the
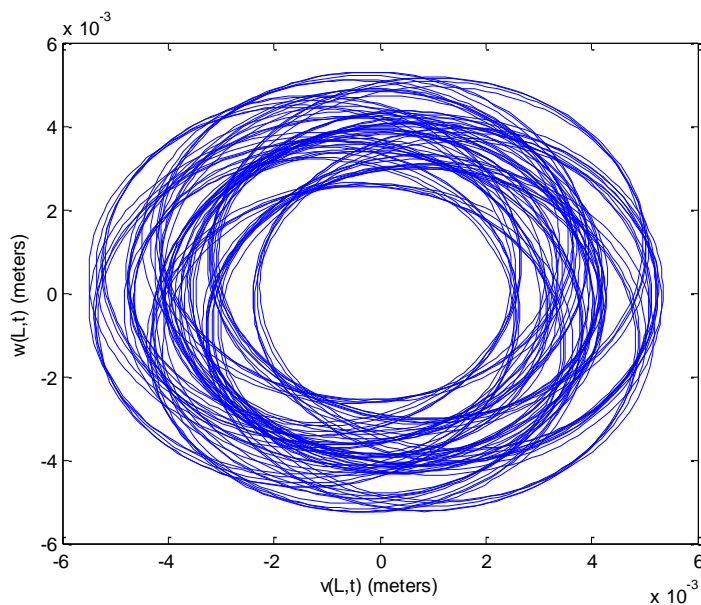
Figure 3.12. Displacement response of drill string when driven at a primary speed of

7.67π rad/s with a secondary frequency addition of 5.75π rad/s.

amplitude response became less circular and its amplitude began to increase. As the secondary frequency increased past 6π rad/s, the response rapidly collapsed back to the shape and amplitude of the base response. The same was true of the system response at 9π and 12.25π rad/s, though the lobe shapes at these peaks in amplitude were different than the one at 6π rad/s. The displacement responses for secondary frequencies of 9π and 12.25π rad/s are depicted in Figure 13.16.

Figure 3.13. Displacement response of drill string when driven at a primary speed of 7.67π rad/s with a secondary frequency addition of 6π rad/s.
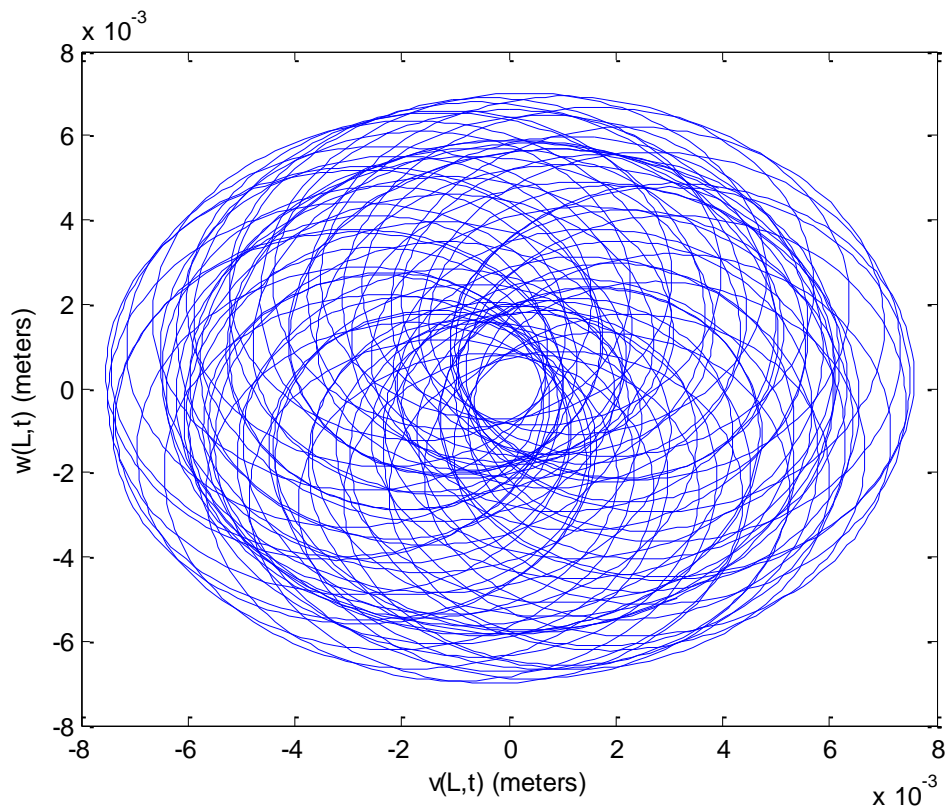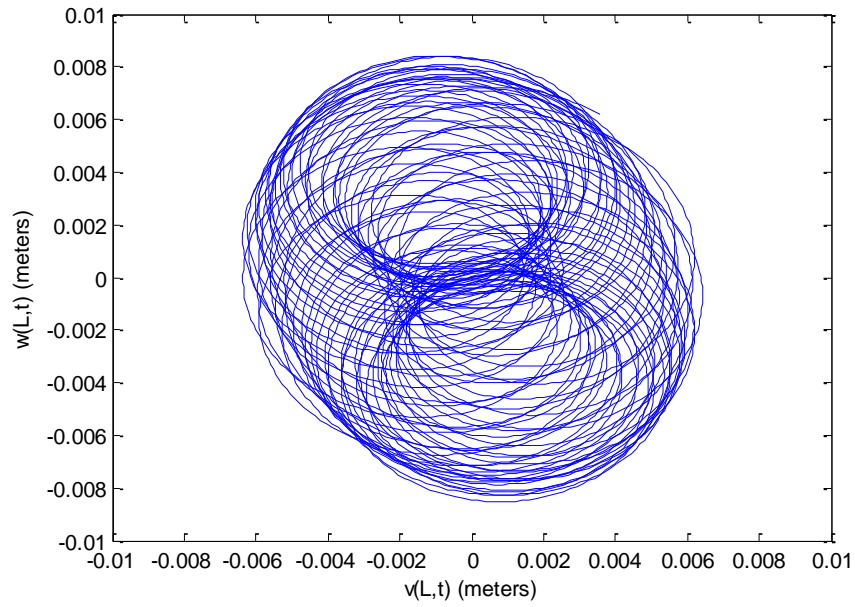
Figure 3.14. Displacement response of drill string when driven at a primary speed of

7.67π rad/s with a secondary frequency addition of 6.25π rad/s.

Figure 3.15. Displacement response of drill string when driven at a primary speed of

7.67π rad/s with a secondary frequency addition of 6.5π rad/s.

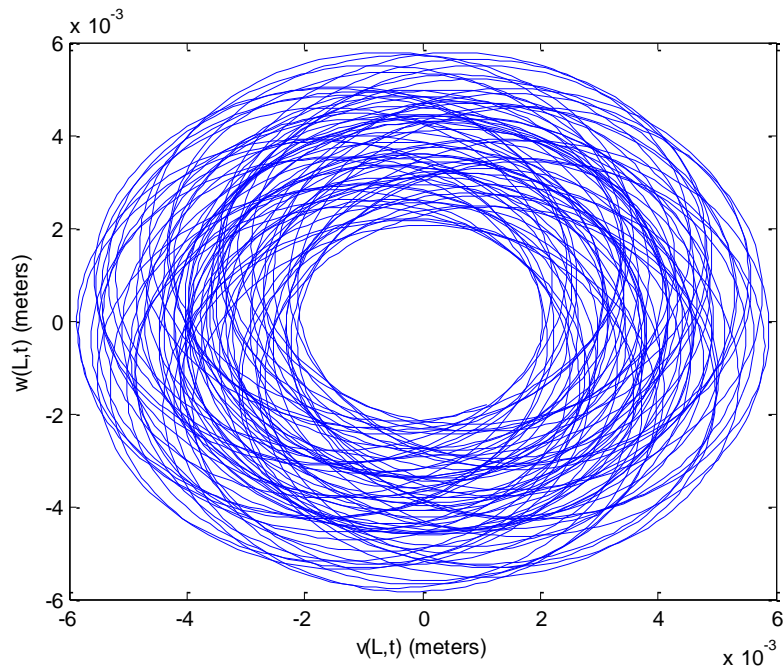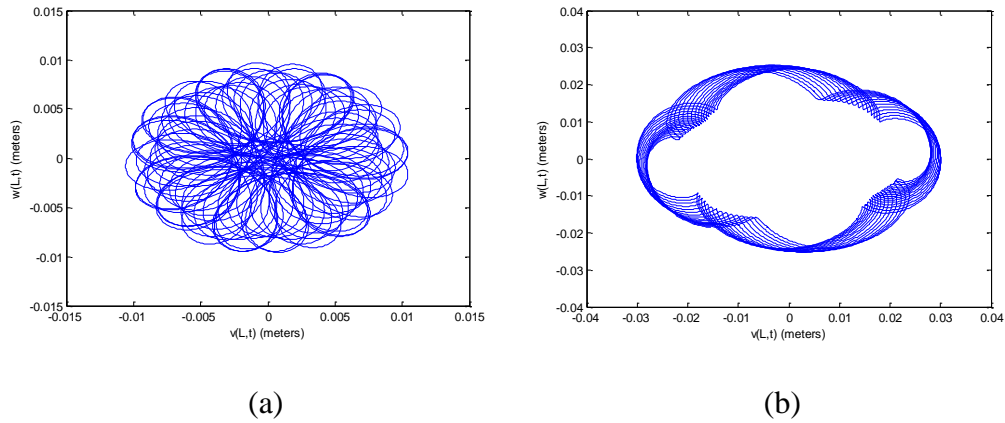**Figure 3.16.** Displacement response of drill string when driven at a primary speed of 7.67π rad/s with a secondary frequency addition: (a) 9π rad/s and (b) 12.25 π rad/s.

The response for the system at a base drive speed of 8π rad/s is shown in Figure 3.17. When the system was driven at a base drive speed of 8π rad/s, the amplitude response of the system was similar to the amplitude response of the system when driven at 7.67π rad/s. Once again the secondary frequency had little effect on the system response outside of a certain set of frequencies. The amplitude response of the system was once again amplified for secondary frequencies near 6π rad/s and 9π rad/s, though the frequencies at which the amplification occur are about 0.25π rad/s higher than those of the system driven at 7.67π rad/s. Interestingly, there is no equivalent peak at secondary frequency of 12 π rad/s between amplitude responses of the system driven at 7.67π rad/s and 8π rad/s.

The lobe shapes of the amplitude response for the system driven at 8π rad/s follow a similar pattern to those of the system drive, with the response prescribing a circle as the baseline response, as depicted in Figure 3.18, and being largely

42
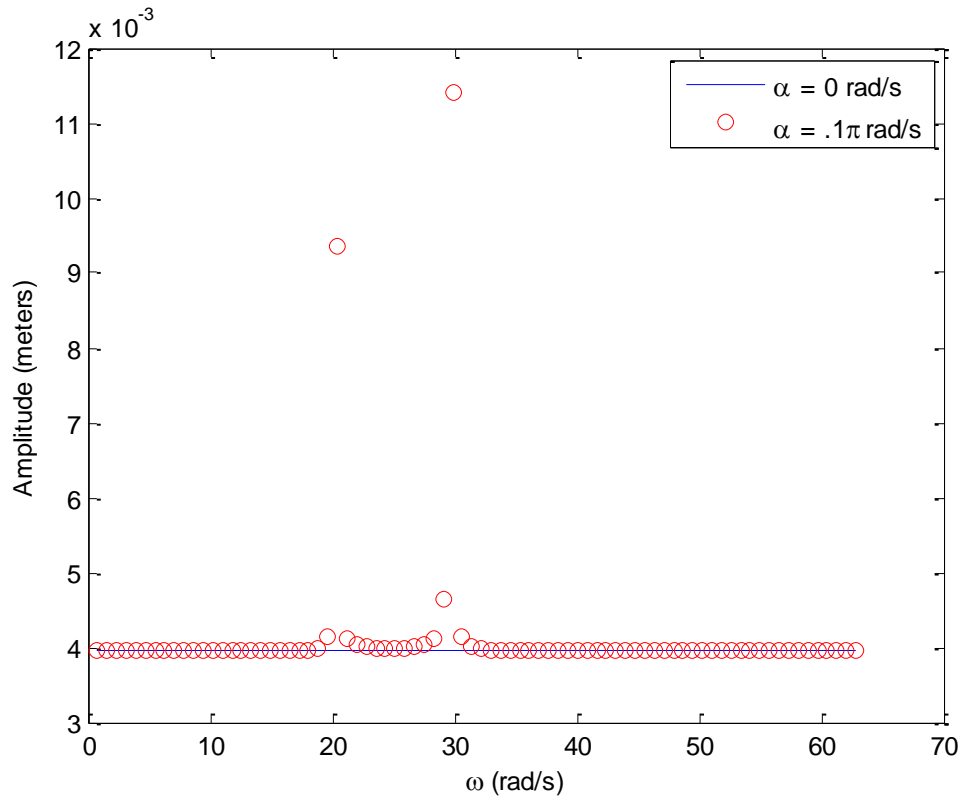
Figure 3.17. Amplitude response of drill string at base drive speed of 8π rad/s.

unaffected by the addition of secondary frequencies, with the exception of the amplifications at secondary frequencies of 6.5π rad/s and 9.5π rad/s. At these peaks in amplitude the lobe shapes of the amplitude responses shift from the consistent circular response to complex periodic or nearly periodic motions, as shown in Figures 3.19 and 3.20b. The shift to these complex lobe shapes is depicted in Figure 3.20, with the lobe shape in Figure 3.20a depicting the transition shape between the peak and the baseline responses.

43
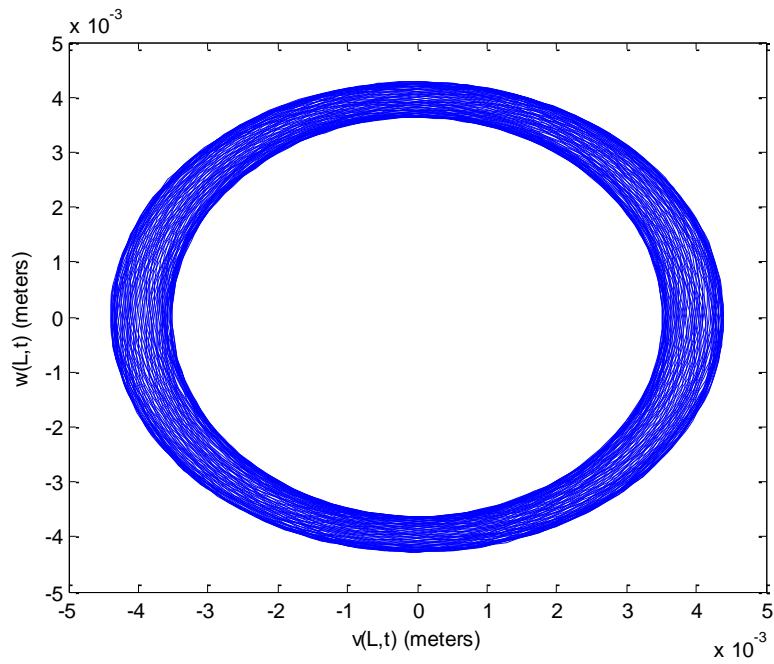
Figure 3.18. Displacement response of drill string when driven at a primary speed of

8π rad/s with no secondary frequency addition.
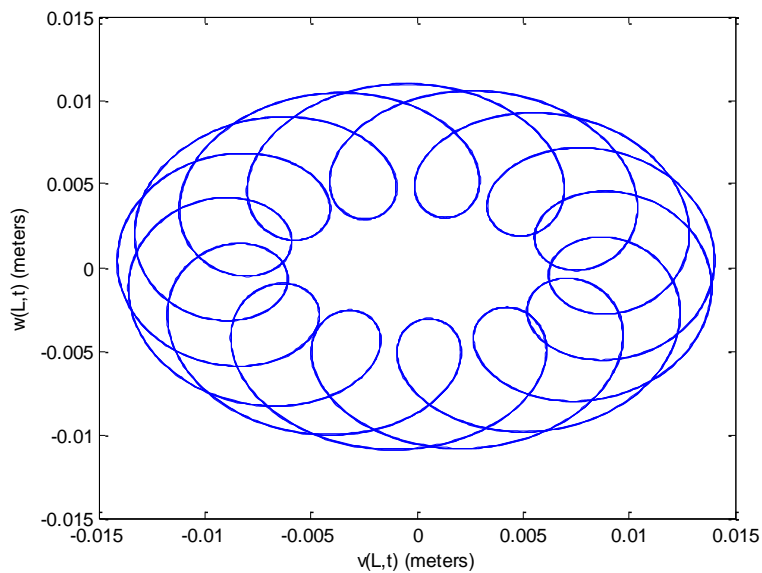
Figure 3.19. Displacement response of drill string when driven at a primary speed of

8π rad/s with a secondary frequency of 6.5π rad/s.

44

(a)   (b)
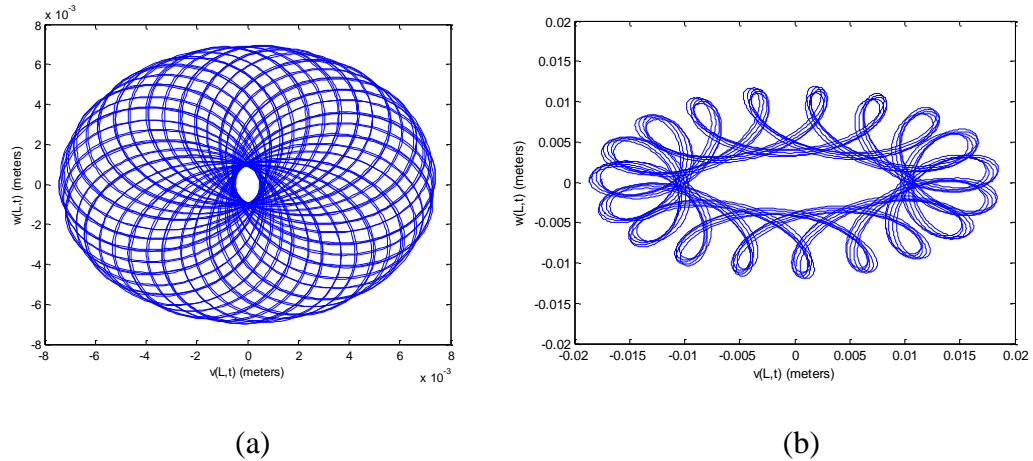
Figure 3.20. Displacement response of drill string when driven at a primary speed of

8π rad/s with a secondary frequency addition: (a) 9.25π rad/s and (b) 9.5π rad/s.

3.6 Comparisons between Experimental and Numerical Results

Overall, the experimental studies and the simulations of the system show

reasonable agreement with one another. The first mode of bending frequency

calculated in the simulations, 1.488π rad/s, is nearly identical to the experimental

determined natural frequency of the system, 1.52π rad/s. The first mode of torsional

frequency for the simulations and the experimental modal, 7.4π and 8.2π rad/s

respectively, are also close. The amplitude responses of the simulation and the

experimental studies are reasonably similar, though the experimental model does

produce some phenomena that does not appear in the simulated system.

In Figures 3.21 below the amplitude response for the experimental model and

simulation for a base drive speed of π rad/s are depicted. The two studies show good

agreement, with both system experiencing a large peak in amplitude for a secondary

frequency of 0.5π rad/s. The decay in amplitude response after the peak amplitudes

for the experimental model are more gradual than those of the simulated model and

45
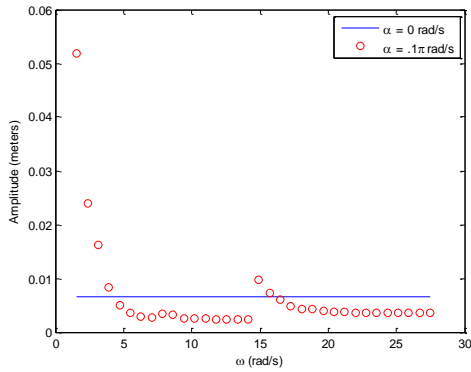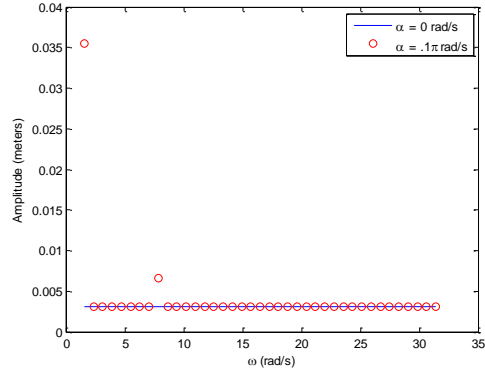
Figure 3.21. Amplitude response of drill string at base drive speed of π rad/s: (a) experiments and (b) simulations.

and the amplitude response for the system eventually attenuates below the baseline response of the system, while the simulation only decays to the baseline response of the system. Both systems also experience a smaller peak as the secondary frequency continues to increase, but the experimental model's peak occurs when the secondary frequency is 4.75π rad/s, while the simulation's is at 2.5π rad/s.

The lobe shapes of the amplitude response for the system when driven at π rad/s show reasonable to excellent correspondence between the experimental studies and the simulations. The baseline response for the systems, shown in Figure 3.22, is circular in both cases, but the lobe shape of the experimental study depicts a large variation in the amplitude over, while the lobe shape of the simulation show very little variant in amplitude. As the systems approach their shared peak when the secondary frequency is 0.5π rad/s, both systems experience a large amplification in amplitude, and the simulation's response becomes as variable at the experimental studies, as shown in Figure 3.23. When the secondary frequency increase to

46

(a)   (b)
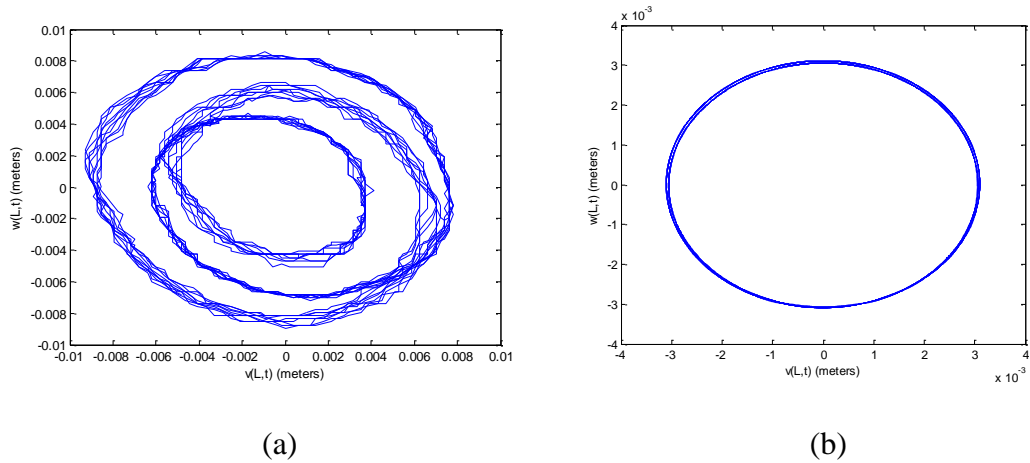
Figure 3.22. Displacement response of drill string when driven at a primary speed of

π rad/s with no secondary frequency addition: (a) experiments and (b) simulations.

(a)   (b)
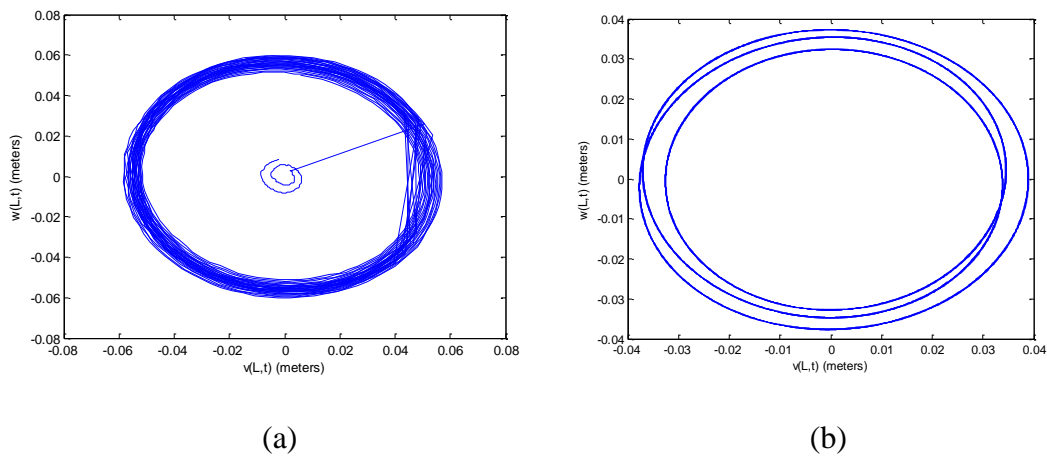
Figure 3.23. Displacement response of drill string when driven at a primary speed of

π rad/s with a secondary frequency of 0.5π rad/s: (a) experiments and (b) simulations.

2. 5π rad/s the simulated system experienced a peak in amplitude due to the lobe

shape of the amplitude response. Though the experimental study does not develop a

similar peak, the lobe shape at this point corresponds very well to the lobe shape of

the simulation, as shown in Figure 3.24. As the secondary frequency is increase past

47

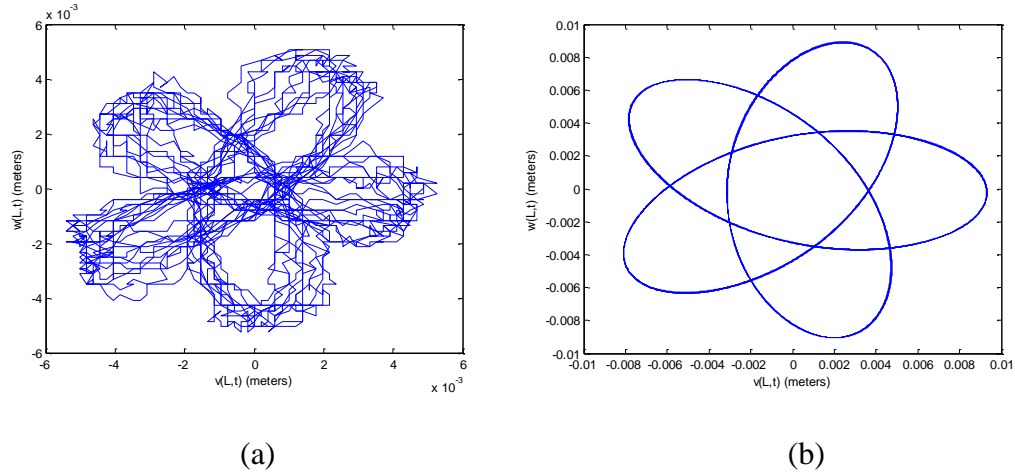(a)   (b)

Figure 3.24. Displacement response of drill string when driven at a primary speed of π rad/s with a secondary frequency of 2.5π rad/s: (a) experiments and (b) simulations.

2.5π rad/s, the decay of the amplitude response takes on a similar form than that of the simulation. The lobe shapes of both the simulation and the experimental studies collapse back to the baseline response of their respective systems, as depicted in Figure 3.25.

(a)   (b)

Figure 3.25. Experimental displacement response of drill string when driven at a primary speed of π rad/s with a secondary frequency of 6π rad/s: (a) experiments and (b) simulations.
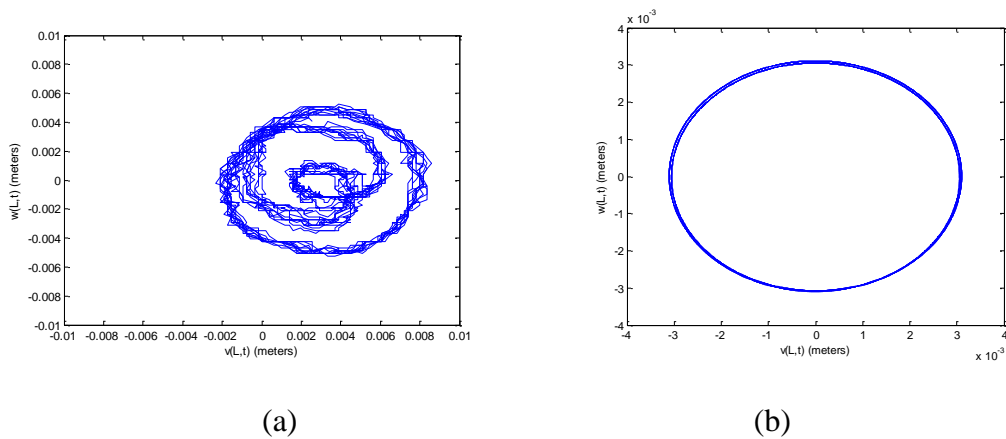
48

The systems' responses for a base drive speed of 1.33π rad/s, displayed in

Figure 3.26, also show good agreement. The overall system responses are very

similar, with the baseline amplitudes being almost identical. Both systems also

experience an amplification in amplitude response for secondary frequencies above π

rad/s, though the amplification for the experimental studies is slightly larger. The

variation in the lobe shape of the amplitude response of the experimental study is also

slightly higher than that of the simulation when the base frequency of the system is

1.33π rad/s. Aside from this increase in variance for the experimental study, the lobe

shapes of the simulation and experimental study show similar behavior. Both system

experience an increase in variance at a secondary frequency of 0.5π rad/s that

collapses back to baseline response shortly as the secondary frequency continues to

increase. This process can be seen in Figures 3.27 – 3.29.

(a)   (b)

Figure 3.26. Amplitude response of drill string at base drive speed of 1.33π rad/s:

(a) experiments and (b) simulations.

49

(a)   (b)
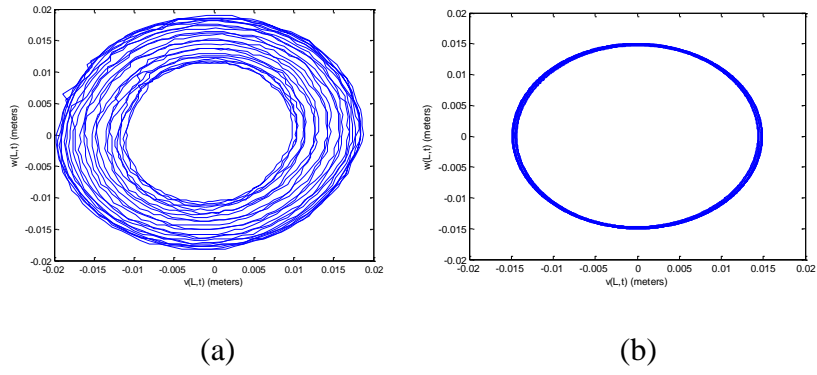
Figure 3.27. Displacement response of drill string when driven at 1.33π rad/s with no

secondary frequency: (a) experiments and (b) simulations.

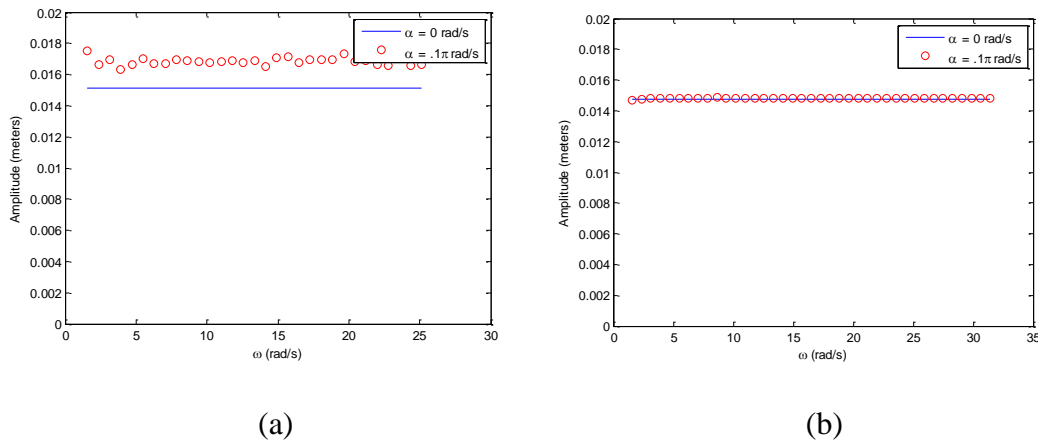(a)   (b)

Figure 3.28. Displacement response of drill string when driven at 1.33π rad/s with a

secondary frequency of 0.5π rad/s: (a) experiments and (b) simulations.

(a)   (b)

Figure 3.29. Displacement response of drill string when driven at 1.33π rad/s with a

secondary frequency of 2π rad/s: (a) experiments and (b) simulations.

The comparisons between the system responses for the experimental studies

and the simulations for base drive speed of 7.67π rad/s and 8π rad/s, presented in

Figures 3.30 and 3.31, show reasonable agreement between the experimental studies

and the simulations and are very similar to one another. In both cases, the simulation

predicts a peak when the secondary frequency is about 6π rad/s that does not occur in

the experimental studies. Both the system driven at 7.67π rad/s and the system driven

at 8π rad/s have circular lobe plots for their baseline responses, with the simulations

and the experimental studies being a good match. This similarity is depicted in

Figures 3.32 and 3.35. Both systems also have a peak at around 9π rad/s, with the

lobe shapes between the experimental studies and the simulation showing good

agreement. This agreement can be observed in Figures 3.33, 3.34, and 3.36.

(a)   (b)

Figure 3.30. Amplitude response of drill string at base drive speed of 7.67π rad/s:

(a) experiments and (b) simulations.
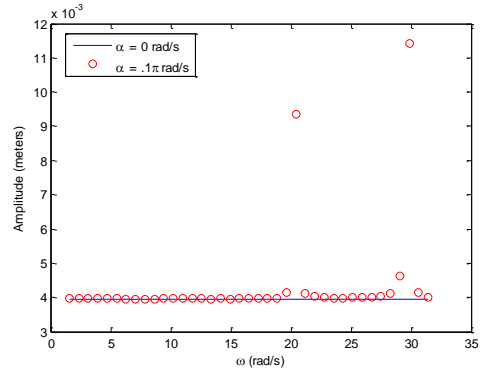
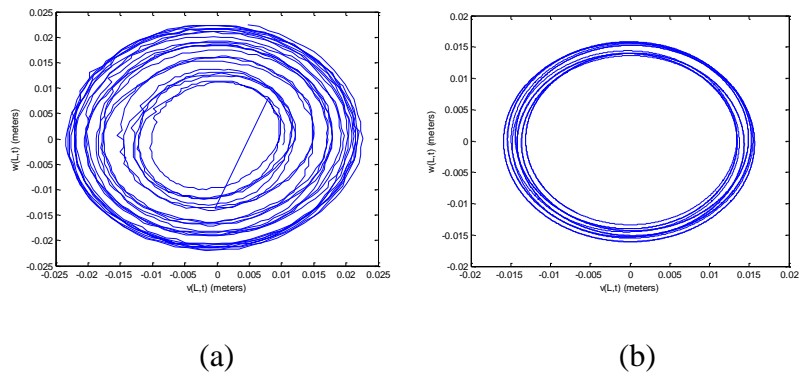(a)   (b)

Figure 3.31. Amplitude response of drill string at base drive speed of 8π rad/s: (a)
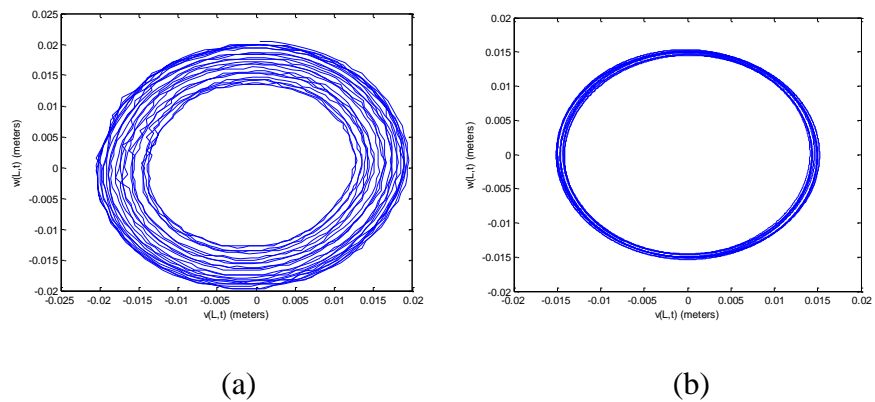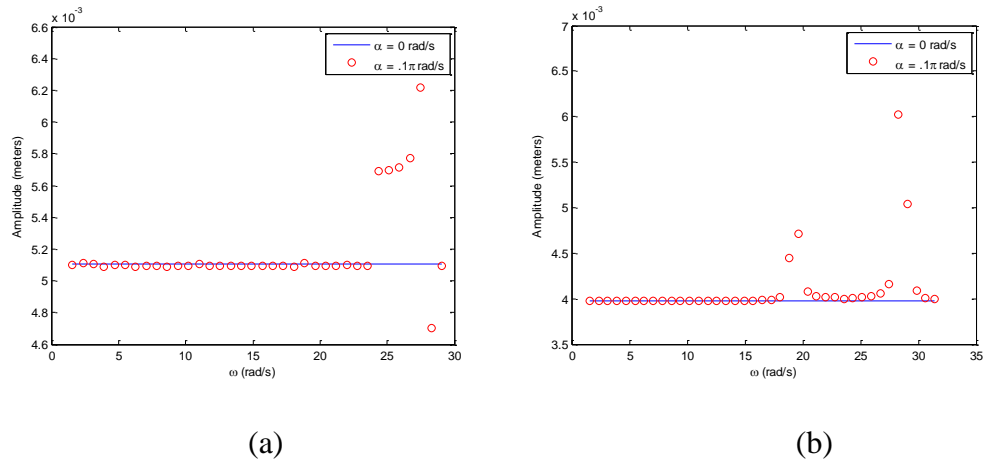
experiments and (b) simulations.
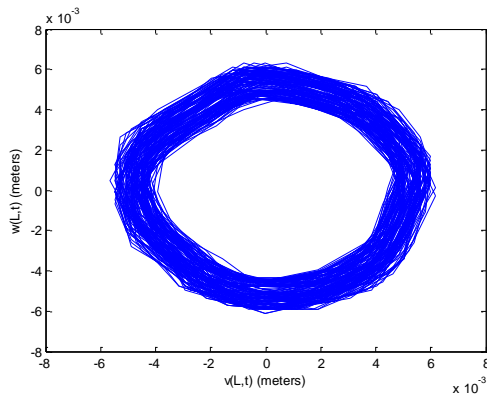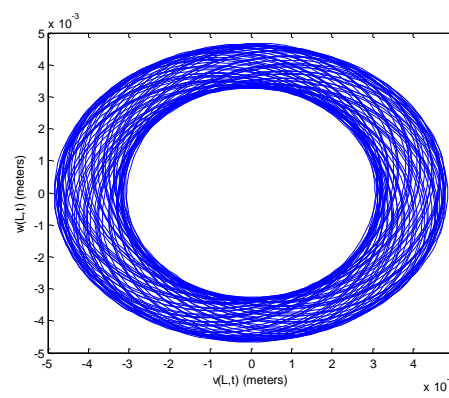
(a)   (b)

Figure 3.32. Displacement response of drill string when driven at 7.67π rad/s with no
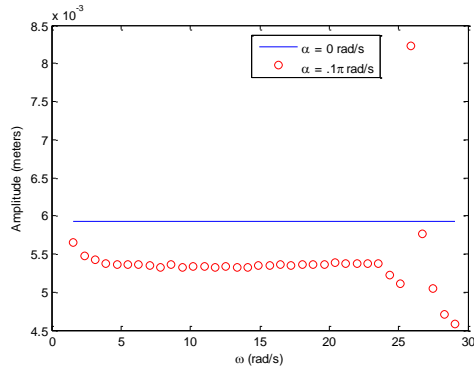
secondary frequency: (a) experiments and (b) simulations.

52
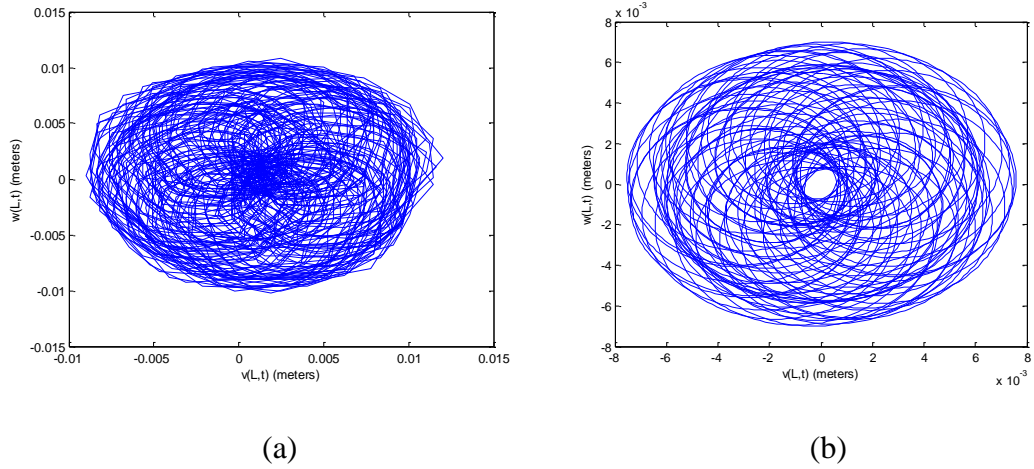
Figure 3.33. Displacement response of drill string when driven at 7.67π rad/s with a

secondary frequency of 2π rad/s: (a) experiments and (b) simulations.
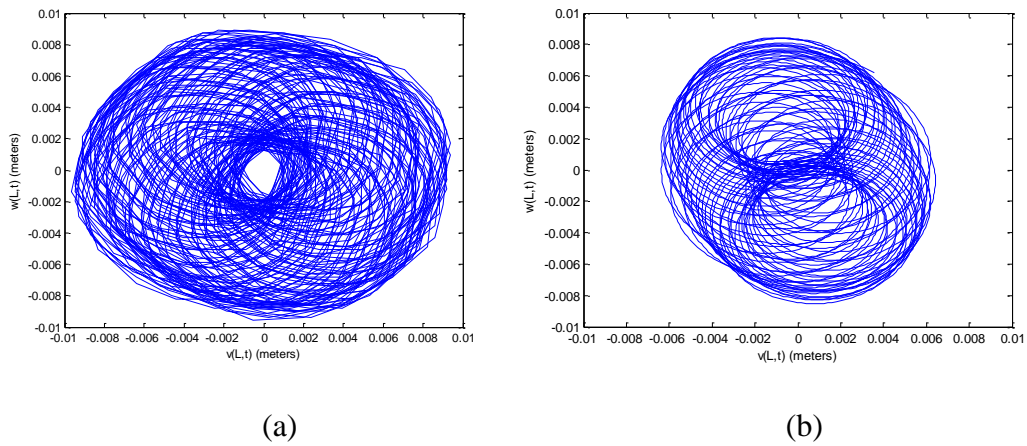
Figure 3.34. Displacement response of drill string when driven at 8π rad/s with a

secondary frequency addition: (a) 9.25π rad/s and (b) 9.5π rad/s.

(a)   (b)
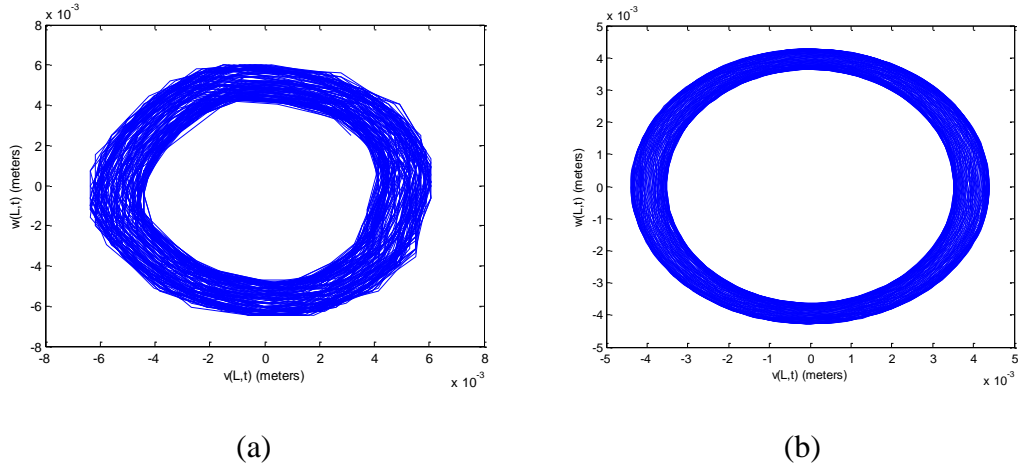
Figure 3.35. Displacement response of drill string when driven at 8π rad/s with no

secondary frequency addition: (a) experiments and (b) simulation.

(a)   (b)
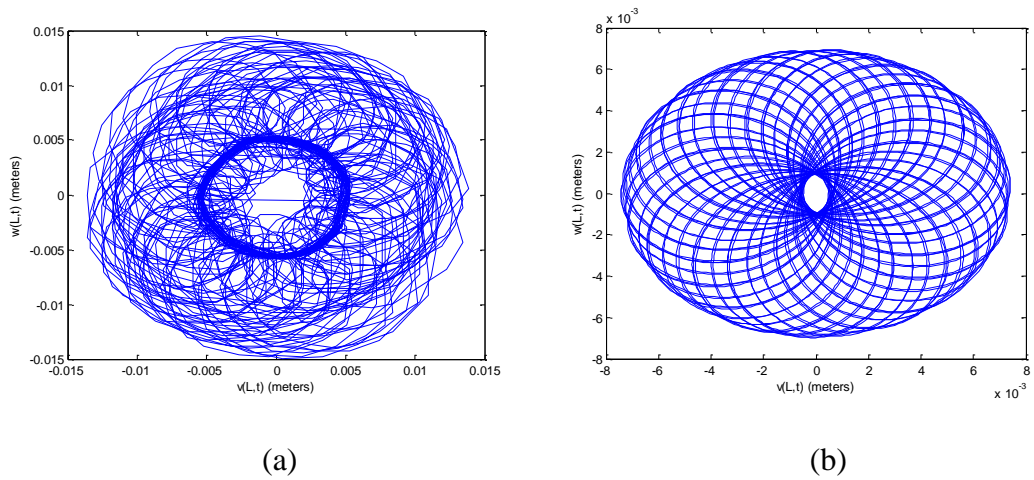
Figure 3.36. Displacement response of drill string when driven at 8π rad/s with a

secondary frequency of 9.25π rad/s: (a) experiments and (b) simulations.

3.7 Preliminary Studies on the effects of the secondary frequency on Rotor-Stator interactions

A preliminary study into the effects of the secondary frequency on the torsional displacement of a system in contact with a borehole wall was conducted in this section in preparation for future work. The parameters used for the force-interaction model from section 3.2 are listed in Table 3.1. The parameters for the structural equations remained the same as those in the experimental studies and simulations. The purpose of the future work that would follow this preliminary study would be to utilize the secondary frequency to control the torsional response of the drill string.

This study was performed with simulation parameters similar to the ones used earlier in the chapter. The two difference are the length of the simulated timespan and the inclusion of the rotor stator interaction forces. The timespan was cut from 1000 seconds to 400 seconds with data being collected for the last 10 seconds instead of 20 seconds, as the rotor-stator interaction causes the system to reach a steady state response more rapidly than it does without said interaction.

Table 3.1. Parameters for Force-Interaction Model

Parameter	Value	Units
K_c	10^6	Nm^{-1}
δ	0.254	m
μ_d	0.07	
μ_s	0.07	
ε_f	10^6	
δ_f	N/A	

In the study, the torsional response of the system was simulated for base drive speeds of π rad/s. The maximum torsional response for the system is shown below in Figure 3.37. The system's torsional response corresponds well amplitude response of the system discussed earlier in the chapter, with peaks in the torsional response corresponding to peaks in the amplitude response. For secondary frequencies at which the system experiences peaks in torsional response, the frequency of torsional oscillation increases greatly compared to the baseline torsional response, while the torsional frequencies where the system does not experience peaks are similar to the baseline torsional response. These frequency interactions are depicted in Figures 3.38 and 3.39
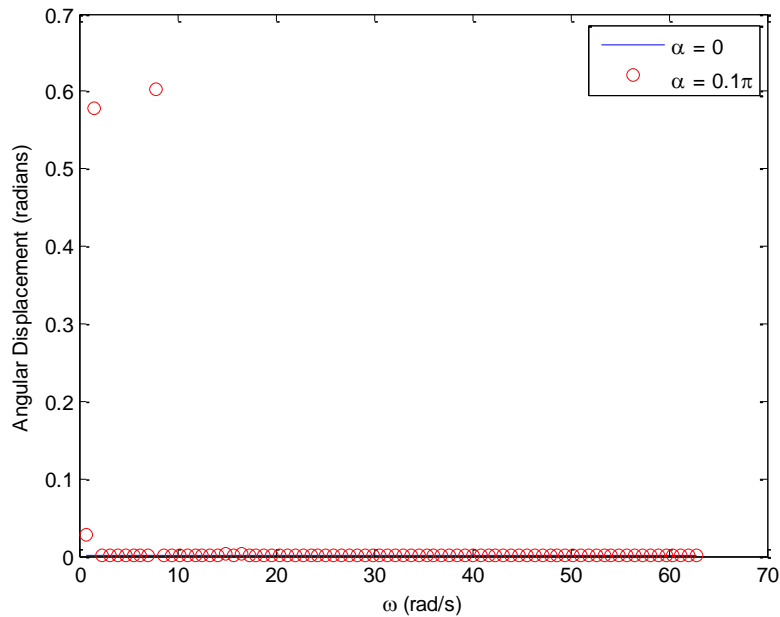
Figure 3.37. Maximum torsional displacement for case with rotor-stator interaction at base drive speed of π rad/s.
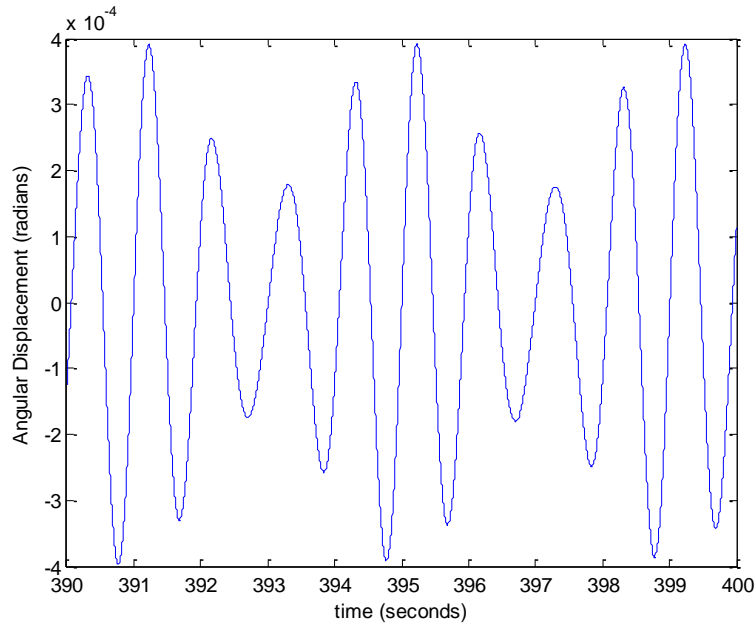
Figure 3.38. Torsional displacement of system when driven at a base drive speed of

1.33π rad/s with a secondary frequency of 0.25π rad/s.
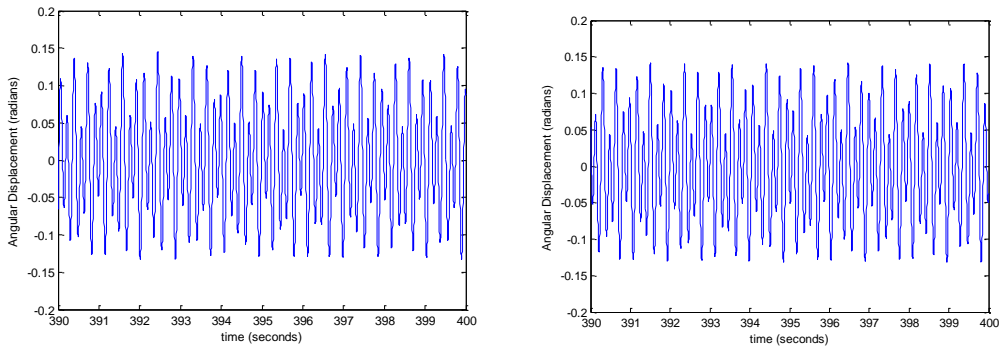
Figure 3.39. Torsional displacement of system when driven at a base drive speed of

π rad/s with a secondary frequency of 0.5π rad/s.

Chapter 4: Concluding Remarks

Drill strings are used extensively in modern drilling operations and these rotating structures can experience high levels of vibrational stress, some of which is due to the string interactions with the borehole wall. These high levels can lead to wear of the drill strings and failure due to fatigue. In an effort to mitigate such failures, many studies have attempted to control the vibrations of drill strings. Typically, this control take the form of a closed loop scheme applied to the drive system. A potential alternative to this type of controller is an open loop scheme based on adding additional input signals into the system in order to attenuate undesirable system responses such as whirling motions. An open loop scheme may not need the expensive sensor arrangements that may be needed for feedback in a closed loop scheme.

This focus of this thesis work has been on investigating the effects of adding a secondary frequency to the drive speed prescribed by a drill string system's motor. In order to develop a control scheme based on adding additional inputs to system, one must first understand how those inputs interact with the system. To this end, experimental studies were performed to determine how a sinusoidal addition to the drive speed of a system would affect its system response. Following earlier work from the author's research group (Vlajic, Liao, Karki, and Balachandran, 2012 and Vlajic, 2014), a model was also developed and the results obtained from this model are compared to those obtained from experimental studies. Finally, a preliminary numerical investigation into the effects of additional secondary frequencies in systems with rotor-stator interactions was performed in preparation for future work.

4.1 Experimental Studies

A rotor-string model of a drill string was fabricated and used to investigate the effects of additional frequency inputs on the amplitude response of a drill string. Secondary frequencies ranging from 0.5π rad/s to 9.25π rad/s were added to base drive speeds near the first bending and torsional mode frequencies of the considered drill string. Of the four base drive speeds studied, namely, π rad/s, 1.33π rad/s, 7.67π rad/s and 8π rad/s, for the drive speed of 1.33π rad/s, no attenuation in amplitude response due to the secondary input was observed. In addition, for the drive speed of 7.67π rad/s, only small attenuations in the amplitude response were noted. At the other base drive speeds, namely, π rad/s and 8π rad/s, the system response amplitude did experience large attenuations due to the addition of the secondary frequency, sometimes decreasing the response to as much as half the baseline response (the case without any secondary input addition). These experimentally observed attenuations support the viability of attenuating undesired system responses by adding an additional frequency input. However, careful consideration of the base drive speeds and secondary frequency additions are needed.

4.2 Simulations and Comparisons with Experimental Studies

The structural and force-interaction model adapted from earlier work by Vlajic, Liao, Karki, and Balachandran (2012) and Vlajic (2014) was used to simulate the system response and comparisons were made with experimental results. On the whole, the numerical results showed reasonable agreement with the experimental results and there were cases with discrepancies as well. The model simulations failed to capture the attenuations of the system response observed in the experimental

studies, and in addition, the model predictions included some behaviors that were not present in the experimental study. This suggests that the model may need further refining to fully explore the dynamics of a drill-string system.

4.3 Suggestions for Future Work

The present thesis works support the possibility of developing an open loop control scheme based on the addition of inputs into the system. However, in order to make this control scheme a reality, there remains much work to be done. First, an in depth study into the effects of secondary frequencies on force interactions between the borehole wall and the drill string must be developed. In addition, a stability analysis needs to be carried out to a better picture of the dynamics of the system. Parametric studies on the effects of altering the secondary frequency and the system's parameters are also recommended with appropriate consideration to models with force interactions as well as those without them. Finally, the model used to simulate the system response can be extended to include higher order modes of the drill-string structure.

Appendix A: Coefficients in Equations of Motion

All terms, which do not have integrals in them, are associated with the position $x=L$.

$$a_1 = [(M + m)\phi_v^2 + I_D\phi_v'^2] \quad (A.1)$$

$$a_2 = 2\zeta_b\sqrt{a_1 a_4} \quad (A.2)$$

$$a_3 = I_{Do}\phi_v'\phi_w' \quad (A.3)$$

$$a_4 = \int_0^L (EI\phi_v''^2 - Mg\phi_v''\phi_v)\, dx + Mg\phi_v'\phi_v \quad (A.4)$$

$$a_5 = I_{Do}\phi_v'\phi_\theta\phi_w' \quad (A.5)$$

$$b_1 = [(M + m)\phi_w^2 + I_D\phi_v'^2] \quad (A.6)$$

$$b_2 = 2\zeta_b\sqrt{b_1 b_4} \quad (A.7)$$

$$b_3 = -I_{Do}\phi_v'\phi_w' \quad (A.8)$$

$$b_4 = \int_0^L (EI\phi_w''^2 - Mg\phi_w''\phi_w)\, dx + Mg\phi_w'\phi_w \quad (A.9)$$

$$b_5 = -I_{Do}\phi_v'\phi_\theta\phi_w' \quad (A.10)$$

$$c_1 = (I_{Do} + me^2)\phi_\theta^2 \quad (A.11)$$

$$c_2 = 2\zeta_t\sqrt{c_1 c_3} \quad (A.12)$$

$$c_3 = GI_o\int_0^L \phi_\theta'^2\, dx \quad (A.13)$$

$$c_4 = I_{Do}\phi_v'\phi_\theta\phi_w' \quad (A.14)$$

Appendix B: Matlab Code

Code used to carry out video analysis

```matlab
file            = 'videoname.avi'
info            = aviinfo(file)
tmov            = mmreader(file);
nFrames         = info.NumFrames;
fRate           = info.FramesPerSecond;
dTime           = 1/fRate;
timeVec         = (0:nFrames-1)*dTime;


positionxPix    = nan(nFrames,1);
positionyPix    = nan(nFrames,1);
adjust          = 1.75;
arealim         = 250;
pix2mm          = 6*2.54*10/(427- 35);


for ind1 = 1:nFrames

    disp(ind1)
    image           = read(tmov,ind1);
    imageCrop       = image;
    level           = graythresh(imageCrop)*adjust;
    imageBW         = im2bw(imageCrop,level);
    [B,L] = bwboundaries(imageBW,4,'noholes');
    s  = regionprops(L);


    for ind2 = 1:length(s);

        if s(ind2).Area > arealim
            positionxPix(ind1)   = s(ind2).BoundingBox(1) +
s(ind2).BoundingBox(3)/2;
            positionyPix(ind1)   = s(ind2).BoundingBox(2) +
s(ind2).BoundingBox(4)/2;
        end
    end
end

positionX       = positionxPix*pix2mm;
positionY       = positionyPix*pix2mm;

[Xcheck] = isnan(positionX);
[Ycheck] = isnan(positionY);


Ncheck = 0;

for ind3 = 1:length(positionX)
    if Xcheck(ind3) == 0 && Ycheck(ind3) ==0
        Ncheck = Ncheck + 1;
        finalX(Ncheck) = positionX(ind3);
        finalY(Ncheck) = positionY(ind3);
    end
end
```

```
meanX            = 90;
meanY            = 84;
positionR        = sqrt((meanX-finalX).^2 + (meanY-finalY).^2);
R_ave(ind5,ind6) = mean(positionR);

NormX=finalX-meanX*ones(length(finalX),1)';
NormY=finalY-meanY*ones(length(finalY),1)';

save([file '_VideoData.mat'])
```

Bibliography

Jansen, J.D. (1991). Non-linear Rotor Dynamics as applied to Oilwell Drillstring Vibrations. *Journal of Sound and Vibration*, *147*(1), 115-135.

Khulief, Y. A., Al-Sulaiman, F.A., & Bashmal, S. (2007). Vibration Analysis of Drillstrings with Self-excited Stick-slip Oscillations. *Journal of Sound and Vibration*, *299*(3), 540-558.

Kreuzer, E., & Struck, H. (2005). Active Damping of Spatio-Temporal Dynamics of Drill-Strings. *IUTAM Symposium on Chaotic Dynamics and Control of Systems and Processes in Mechanics Solid Mechanics and its Applications*, *122*, 407-417.

Liao, C.-M. (2011). Experimental and Numerical Studies of Drill-String Dynamics, PhD Dissertation, University of Maryland, College Park, MD.

Liao, C.-M., Balachandran, B., Karkoub, M., & Abdel-Magid, Y. L. (2011). Drill-String Dynamics: Reduced-Order Models and Experimental Studies. *Journal of Vibration and Acoustics*, *133*(4), 041008-041015.

Melakhessou, H., Berlioz, A., & Ferraris, G. (2003). A Nonlinear Well-Drillstring Interaction Model. *Journal of Vibration and Acoustics*, *125*(1), 46-52.

Sampaio, R., Piovan, M.T., & Lozano, G. V. (2005). Non-linear model for coupled axial/torsional vibrations of drill-strings. Proceedings of COBEM 2005, Ouro Preto, MG. ABCM, November 6-11.

Sampaio, R., Piovan, M.T., & Lozano, G. V. (2007). Coupled axial/torsional vibrations of drill-strings by means of non-linear model. *Mechanics Research Communications*, *34*(5-6), 497-502.

Serrarens, A., van de Molengraft, Kok, J.J., & van den Steen, L. (1998). H∞ control for suppressing stick-slip in oil well drillstrings. *IEEE Control Systems Magazine*, *18*(2), 19-30.

Tucker, R. W. & Wang, C. (2003). Torsional Vibration Control and Cosserat Dynamics of a Drill-Rig Assembly. *Meccanica*, *38*(1), 143-159.

Tucker, W. R. & Wang, C. (1999). On the Effective Control of Torsional Vibrations in Drilling Systems. *Journal of Sound and Vibration*, *224*(1), 101-122.

Tucker, W. R. & Wang, C. (1999). An Integrated Model for Drill-String Dynamics. *Journal of Sound and Vibration*, *224*(1), 123-165.

Vlajic, N., Liao, C.M., Karki, H., & Balachandran, B. (2012). Rotor Torsion Vibrations in the Presence of Continuous Stator Contact. Proceedings of ASME IMECE2012, Houston, TX doi: 10.1115/IMECE2012-891895, November 9—15.

Vlajic, N. (2014). Dynamics of Slender, Flexible Structures. PhD Dissertation, University of Maryland, College Park, MD

Yigit, A. S., & Christoforou, A. P. (2000). Coupled Torsional And Bending Vibrations of Actively Controlled Drillstrings. *Journal of Sound and Vibration*, *234*(1), 67-83.

Yigit, A. S. & Christoforou, A. P. (2006). Stick-Slip and Bit-Bounce Interaction in Oil-Well Drillstrings. *Journal of Energy Resources Technology*, *128*(4), 268-274.